# Evaluation of aerosol properties over ocean from Moderate Resolution Imaging Spectroradiometer (MODIS) during ACE-Asia

D. A. Chu,[1,2] L. A. Remer,[3] Y. J. Kaufman,[3] B. Schmid,[4] J. Redemann,[4]
K. Knobelspiesse,[5,6] J.-D. Chern,[3,7] J. Livingston,[4] P. B. Russell,[4] X. Xiong,[8]
and W. Ridgway[5,2]

[1]   The Aerosol Characterization Experiment-Asia (ACE-Asia) was conducted in March−May 2001 in the western North Pacific in order to characterize the complex mix of dust, smoke, urban/industrial pollution, and background marine aerosol that is observed in that region in springtime. The Moderate Resolution Imaging Spectroradiometer (MODIS) provides a large-scale regional view of the aerosol during the ACE-Asia time period. Focusing only on aerosol retrievals over ocean, MODIS data show latitudinal and longitudinal variation in the aerosol characteristics. Typically, aerosol optical depth ($\tau_a$) values at 0.55 $\mu$m are highest in the $30°−50°$ latitude band associated with dust outbreaks. Monthly mean $\tau_a$ in this band ranges $\sim 0.40−70$, although large differences between monthly mean and median values indicate the periodic nature of these dust outbreaks. The size parameters, fine mode fraction ($\eta$), and effective radius ($r_{eff}$) vary between monthly mean values of $\eta = 0.47$ and $r_{eff} = 0.75$ $\mu$m in the cleanest regions far offshore to approximately $\eta = 0.85$ and $r_{eff} = 0.30$ $\mu$m in near-shore regions dominated by biomass burning smoke. The collocated MODIS retrievals with airborne, ship-based, and ground-based radiometers measurements suggest that MODIS retrievals of spectral optical depth fall well within expected error ($\Delta\tau_a = \pm 0.03 \pm 0.05\tau_a$) except in situations dominated by dust, in which cases MODIS overestimate both the aerosol loading and the aerosol spectral dependence. Such behavior is consistent with issues related to particle nonsphericity. Comparisons of MODIS-derived $r_{eff}$ with AERONET retrievals at the few occurrences of collocations show MODIS systematically underestimates particle size by 0.2 $\mu$m. Multiple-year analysis of MODIS aerosol size parameters suggests systematic differences between the year 2001 and the years 2000 and 2002, which are traced to instrumental electronic cross talk. Sensitivity studies show that such calibration errors are negligible in $\tau_a$ retrievals but are more pronounced in size parameter retrievals, especially for dust and sea salt.

**Citation:**  Chu, D. A., et al. (2005), Evaluation of aerosol properties over ocean from Moderate Resolution Imaging Spectroradiometer (MODIS) during ACE-Asia, *J. Geophys. Res.*, *110*, D07308, doi:10.1029/2004JD005208.

## 1.  Introduction

[2]   For over two decades much research has been devoted to studies of the effects of Saharan dust on the Earth's radiative balance [*Carlson and Benjamin*, 1980; *Tegen and Fung*, 1994, 1995; *Tegen et al.*, 1996; *Li et al.*, 1996; *Andreae*, 1996; *Hsu et al.*, 2000; *Haywood et al.*, 2003], atmospheric chemistry [*Dentener et al.*, 1996], and biogeochemical cycle [*Swap et al.*, 1992]. In contrast, Asian dust has received much less scrutiny by the global community. In Asia, although dust storms occur year-round in the source region, dust outbreaks appear to be the strongest in springtime based upon 40 years ground observations [*Sun et al.*, 2001]. However, it has been a difficult task to characterize composition of the Asian dust outbreaks because the air mass includes not only dust particles but the growing and variable sources of the precursors of water soluble aerosols, such as $NO_x$ and $SO_2$ gases [*Elliot et al.*, 1997; *VanArdeen*

---

[1]Joint Center for Earth Systems Technology, University of Maryland Baltimore County, Baltimore, Maryland, USA.

[2]Also at Laboratory for Atmospheres, NASA Goddard Space Flight Center, Greenbelt, Maryland, USA.

[3]Laboratory for Atmospheres, NASA Goddard Space Flight Center, Greenbelt, Maryland, USA.

[4]NASA Ames Research Center, Moffett Field, California, USA.

[5]Science Systems and Applications, Inc., Lanham, Maryland, USA.

[6]Also at Laboratory for Hydrology, NASA Goddard Space Flight Center, Greenbelt, Maryland, USA.

[7]Also at Goddard Earth Sciences and Technology Center, University of Maryland Baltimore County, Baltimore, Maryland, USA.

[8]Laboratory for Terrestrial Physics, NASA Goddard Space Flight Center, Greenbelt, Maryland, USA.
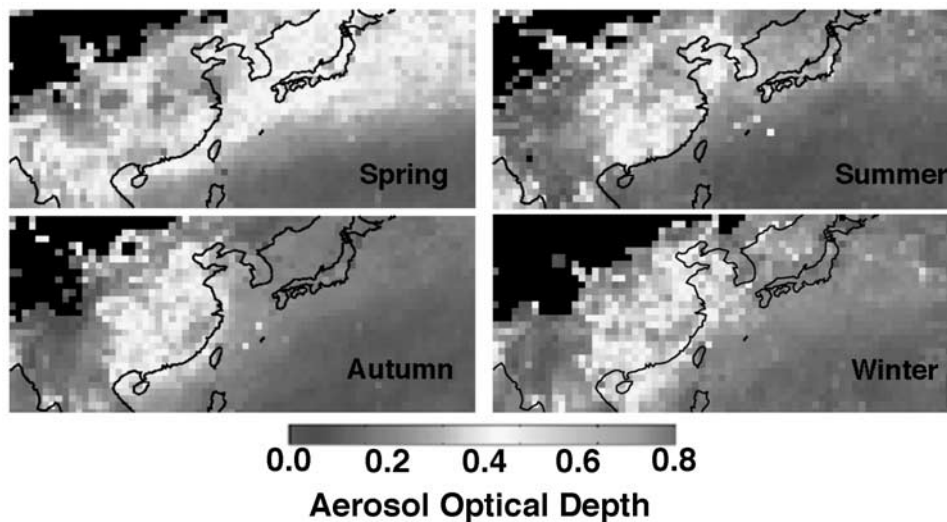
**Figure 1.** Seasonal mean $\tau_a$ in spring, summer, autumn, and winter (December 2000 to November 2001) for the region of $15°-45°$N and $90°-160°$E. See color version of this figure at back of this issue.

*et al.*, 1999]. A multinational, multiplatform field campaign, so-called the Aerosol Characterization Experiment, Asia (ACE-Asia), was therefore planned and executed in March–May 2001 to study aerosol physical, chemical, and radiative properties in east Asia and the western Pacific Ocean [*Huebert et al.*, 2003].

[3] Asian dust storms rising from the Taklimakan and Gobi deserts (as well as neighboring areas), sweeping through east Asia are closely associated with frontal development and Mongolian cyclonic depressions. The dust-laden air mass can travel long distance reaching as far as the United States and beyond. Drought in northern and northwestern China is believed to play a critical role in the increasing frequency, intensity, duration, and area of occurrence of dust outbreaks in the past few years. In addition, the loss of vegetation due to agricultural and livestock breeding activities (e.g., at a rate of 400 million $km^2$ per year) in northwestern China has also contributed significantly to the total dust emission of 800 million tons annually. In spring 2001, 3 strong, 10 moderate, and 5 weak outbreaks occurred in northern China with 41 dusty days recorded in the region. Unlike Saharan dust storms dominated by dust particles, Asian dust clouds are often mixed with urban/industrial pollutants. By serving as the reactive surface, dust particles can modify chemical processes of the formation of acid gases (e.g., $H_2SO_4$ and $HNO_3$) [*Tabazadeh et al.*, 1998; *Goodman et al.*, 2000; *Phadnis and Carmichael*, 2000; *Terada et al.*, 2002]. Biomass burning from Southeast Asia, as a result of agricultural cleaning, is responsible for emitting significant amounts of soot to the atmosphere. The smoke plumes carried by the southwesterlies can mix with pollution (and dust) over the western Pacific Ocean before reaching further downwind regions. It is evident that elevated CO ($\sim$10%), $PM_{10}$ ($\sim$50%) and PAN (Peroxyacetylnitrate) ($\sim$100%) concentrations were observed in the free atmosphere in western US during springtime [*Jaffe et al.*, 1999].

[4] The purpose of this paper is to evaluate the accuracy of MODIS-derived aerosol properties ($\tau_a$, $\eta$ and $r_{eff}$) over the western Pacific Ocean in March–May 2001 during the

ACE-Asia field campaign. As found, dust nonsphericity and MODIS sensor calibration issues in shortwave infrared (SWIR) further complicate the columnar aerosol retrieval with variable aerosol sources (dust, pollution, and smoke) and vertical distributions. Terra-MODIS sensor electronics was switched from side A to side B (for better ocean color retrieval from less noisy ocean bands) on 30 October 2000 and later switched back to side A on 2 July 2001 (after side B power supply failed in mid-June). Though similar optical calibrations were done prior to and post the switch, the level 1B (L1B) SWIR (i.e., 1.24, 1.64, and 2.1 $\mu$m) band radiances could be different due to the out-of-band thermal leak ($3-5$ $\mu$m) and electronic cross talk (residual electrons from imperfect detector reset of the 500 m resolution subframes) [*Xiong et al.*, 2003]. The differences may have caused the anomalies in the MODIS-derived size parameters since the weighting between the fine and coarse mode aerosols obtained in the retrieval is attributed to the spectral curvature of measurements from the visible (i.e., 0.55, 0.66, 0.87 $\mu$m without thermal leak and electronic cross talk) all the way through the SWIR bands. The details of the derivation of $\tau_a$, $\eta$ and $r_{eff}$ using the visible-SWIR bands are documented in the work of *Remer et al.* [2005]. In section 2, we briefly describe MODIS aerosol retrieval algorithm over ocean and the expected accuracies of retrieved parameters. In section 3, we analyze the latitudinal and regional distribution and variation as a preview before validation.

[5] The multiplatform based Sun photometers and radiometers from the C-130 and Twin Otter airplanes, NOAA R/V *Ronald Brown*, and AERONET (Aerosol Robotic Network) provide a suite of ground truths to validate MODIS $\tau_a$ retrievals. Of particular importance are the AATS-14 (14-channel Ames Airborne Tracking Sun photometer) measurements at 1.24 and 1.64 $\mu$m since the longer wavelengths are more sensitive to the existence of large particles such as dust. The detailed comparisons of (collection 4) MODIS-derived $\tau_a$ (assuming spherical particles) against the Sun photometer/radiometer observations from
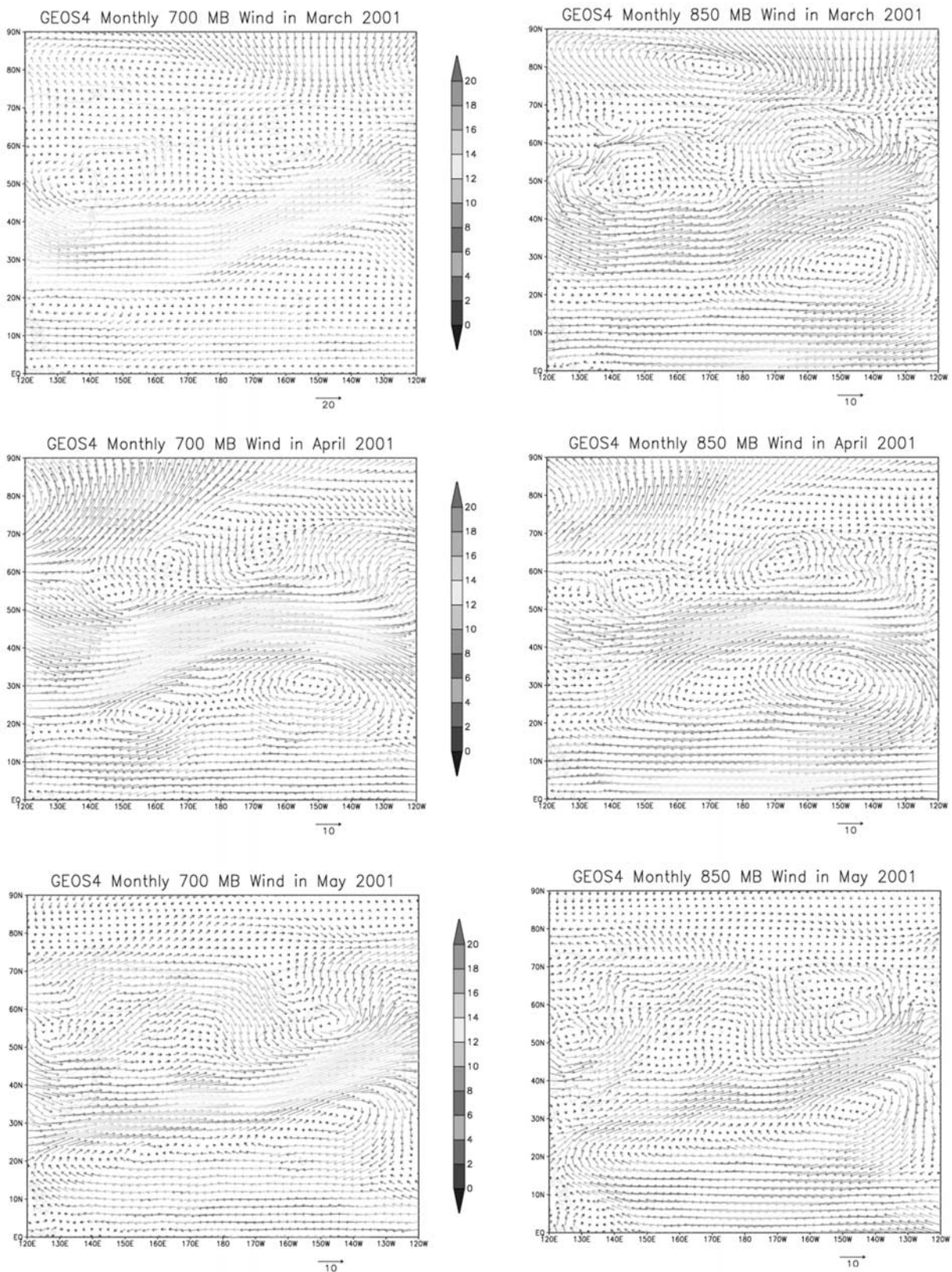
**Figure 2.** NASA Global Modeling and Assimilation Office (GMAO) (formerly the Data Assimilation Office) assimilated winds at 700 (left column) and 850 mb (right column) for (top) March, (middle) April, and (bottom) May 2001. See color version of this figure at back of this issue.
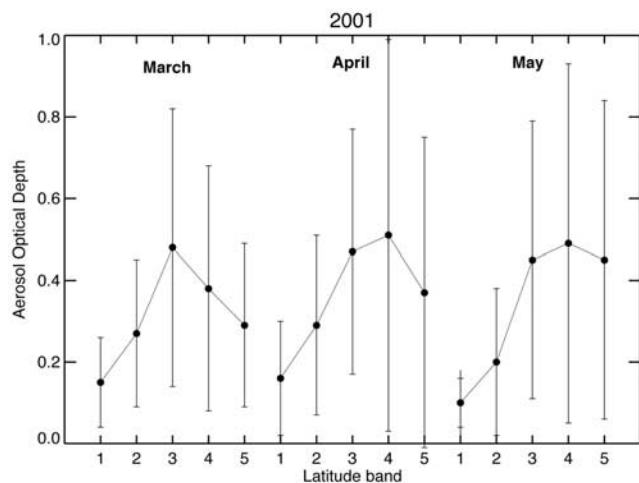
**Figure 3.** Monthly zonal mean $\tau_a$ calculated in different latitude bands (1, $10°-20°N$; 2, $20°-30°N$; 3, $30°-40°N$; 4, $40°-50°N$; 5, $50°-60°N$) in March, April, and May 2001.

the visible to SWIR bands are shown in section 4. Dust nonsphericity is critical to $\tau_a$ retrieval of dust. To model the effect, however, requires information of dust phase functions of the entire MODIS bands from visible to SWIR, which are currently lacking. These studies are ongoing and thus excluded in this paper.

[6] In section 5, we discuss the validation of $r_{eff}$ using AERONET sky measurements observations and $\eta$ from currently ongoing research. In section 6, we analyze the consistency/relationship between retrieved size parameters (i.e., $r_{eff}$, $\eta$ and Ångström Exponents) and corresponding aerosol models based upon the cases in sections 4.1 and 4.2. Dust nonsphericity and electronic cross talk have a compounding effect on the retrieved $r_{eff}$ that both tend to underestimate $r_{eff}$. In section 7, we make an attempt to mimic the responses of retrievals due to electronic cross-talk effect by imposing a uniform changes ($-5\%$ to $5\%$) on the SWIR band radiances. In section 8, a statistical analysis is used to estimate the discrepancies of $r_{eff}$ and $\eta$ between the retrievals of 2001 (side B electronics) and those of 2000 and 2002 (side A electronics). The systematically larger (smaller) $\eta$ ($r_{eff}$) values derived with side B electronics, and associated higher degree of severity found in low than high aerosol loading and in coarse-mode than fine-mode dominated regions indicate the nonlinearity in nature of electronic cross talk. Unless the cross talk effect can be completely removed or fully characterized, the evaluation of the uncertainties of MODIS-derived aerosol size parameters remains inconclusive in ACE-Asia.

## 2. MODIS Aerosol Retrieval Over Ocean and Expected Accuracies

[7] The MODIS aerosol retrieval algorithm is composed of two different schemes in retrieving aerosol properties over land and ocean. The details of the algorithm can be found in the work of *Kaufman et al.* [1997] and *Chu et al.* [1998] (land) and *Tanré et al.* [1997, 1999] (ocean). The enhancements and modifications of the schemes for gener-

ating different MODIS collections were described in the work of *Chu et al.* [2003] (land), *Levy et al.* [2003] (ocean) and *Remer et al.* [2005] (land and ocean). Here, we briefly describe the methodology and processes used for retrieving aerosol properties over ocean. The aerosol ocean algorithm employs six MODIS 500 m spectral bands (0.55, 0.67, 0.86, 1.24, 1.64, and 2.1 μm) to retrieve aerosol properties including aerosol optical depth, fine-mode fraction, and effective radius etc. within $10 \times 10$ km$^2$ grid box (nadir) under the cloud-free and glint-free conditions (e.g., glint angle > 40°). Three procedures are executed in order to obtain "clear" pixels for aerosol retrieval. Cloud screening is first performed, including the spatial variability tests (0.55 μm reflectance measurements) [*Martins et al.*, 2002], brightness temperature tests (6.7, 11, and 12 μm) [*Ackerman et al.*, 1998], and 1.38 and 0.66 μm reflectance and reflectance ratio of 1.38/1.24 μm tests [*Gao et al.*, 2002]. The latter is to remove high and thin cirrus clouds. A sediment mask is applied subsequently to discard pixels of reflection enhanced by river sediments around river months [*Li et al.*, 2003]. The remaining (cloud-free, glint-free, and sediment-free) pixels of a total of 400 pixels ($20 \times 20$ at 500 m resolution in $10 \times 10$ km$^2$ box) are then sorted in ascending order to further remove the 25% darkest and brightest pixels to exclude possible residual cloud, glint, and cloud-shadow contaminations. Given the "clear" pixels within $10 \times 10$ km$^2$ grid box, a least residual method [*Tanré et al.*, 1997] is used to determine the fraction of fine and coarse mode aerosol models by minimizing the differences of six-paired measured and calculated spectral radiances (0.55–2.1 μm) of 20 combinations of 4 fine-mode and 5 coarse-mode aerosol models. For the best scenario, the normalized residual is expected to be less than 3% with optimal retrieval quality. For other cases, the retrieved aerosol properties need to take into account the processing paths permitted in less ideal conditions (e.g., cloud screening, missing spectral channels, etc.). The details of quality assessment (QA) of retrieval can be found in MODIS Atmosphere QA Plan [*Chu et al.*, 2002] (http://modis-atmos.gsfc.nasa.gov). The major aerosol parameters retrieved over ocean include spectral aerosol optical depths (0.47–2.1 μm), Ångström exponents, fine-mode fraction, and effective radius. The secondary parameters such as reflected/transmitted fluxes, CCN (Cloud Condensation Nuclei), columnar mass concentration are obtained from lookup tables.

[8] Despite that MODIS reports aerosol optical depths at seven wavelengths over ocean, only 0.66 μm and 0.87 μm channels are sufficiently similar in wavelength for direct comparison with AERONET Sun photometer measurements. Based upon the recent validation [*Remer et al.*, 2002, 2005], the retrieval errors of aerosol optical depth are found within $\Delta\tau_a = \pm 0.03 \pm 0.05\tau_a$, which can be translated to a standard error of $\sim 0.02$, which is a half of that reported for AVHRR $\sim 0.04$ [*Stowe et al.*, 1997]. In terms of particle size, the validation of MODIS versus AERONET-derived effective radius reveals approximately 70% of 25 colocated points falls within $\pm 0.1$ μm (or 25% error) for $\tau_a$ (0.66 μm) > 0.15. Larger errors are expected for $\tau_a$ (0.66 μm) < 0.15, because of greater susceptibility to algorithmic and sensor uncertainties [*Ignatov et al.*, 1998]. AERONET-derived effective radius use sky radiance and $\tau_a$
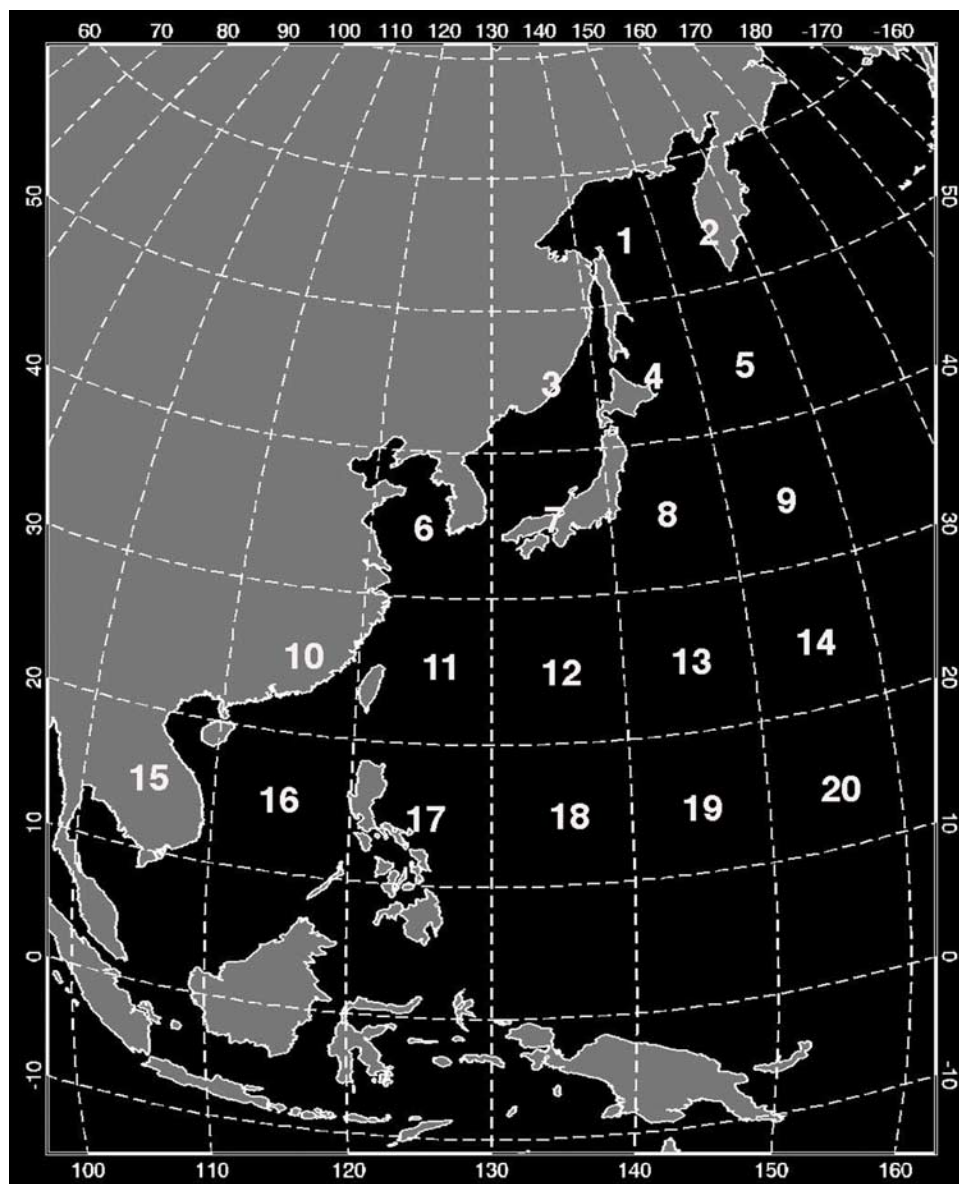
**Figure 4.** Twenty $10° \times 10°$ regions of the domain of ACE-Asia 2001.

data to derive the aerosol size distributions, from which the effective radius is calculated [*Dubovik and King*, 2000]. The similarity of both derived from total column ambient observations makes MODIS and AERONET directly comparable. It is worth noting that in the work of *Remer et al.* [2002] none of the validation points was derived from dust observations. The validation done by *Levy et al.* [2003] during PRIDE (The Puerto Rico Dust Experiment) showed that the assumption of sphericity is responsible for creating errors in dust retrieval, leading to overestimated $\tau_a$ at 0.47 and 0.55 μm and underestimated particle sizes (~50% in general and a factor of 2 to 3 in some cases).

## 3.  Latitudinal and Regional Analyses

[9] Elevated aerosol loading attributed to Asian dust outbreaks and biomass burning is clearly seen in the Northern Hemisphere in springtime. Figure 1 depicts the seasonal mean $\tau_a$ of the area between $15°-45°$N and $90°-160°$E of interest in the ACE-Asia experiment. High aerosol abundance is worth noting in all seasons in the Sichuan basin, on the eastern coast, and in northern and southern China as a result of urban/industrial pollution. In spring, April shows the largest regional monthly average $\tau_a$ (~$0.45 \pm 0.40$), in which dust outbreak has contributed significantly to aerosol loading, followed by March (~$0.40 \pm 0.33$) and May (~$0.40 \pm 0.40$).

[10] Based upon 40-year ground observations [*Sun et al.*, 2001], the dust transport routes can be summarized into three latitude bands (frequency of occurrence is denoted in the parentheses): (1) $40°-70°$N (7%), (2) $30°-40°$N (60%), and (3) $0°-30°$N (33%). Set up by a low-pressure system over the Aleutian Islands and a high-pressure cell near Hawaii, the meteorological scenario so-called "The Asian

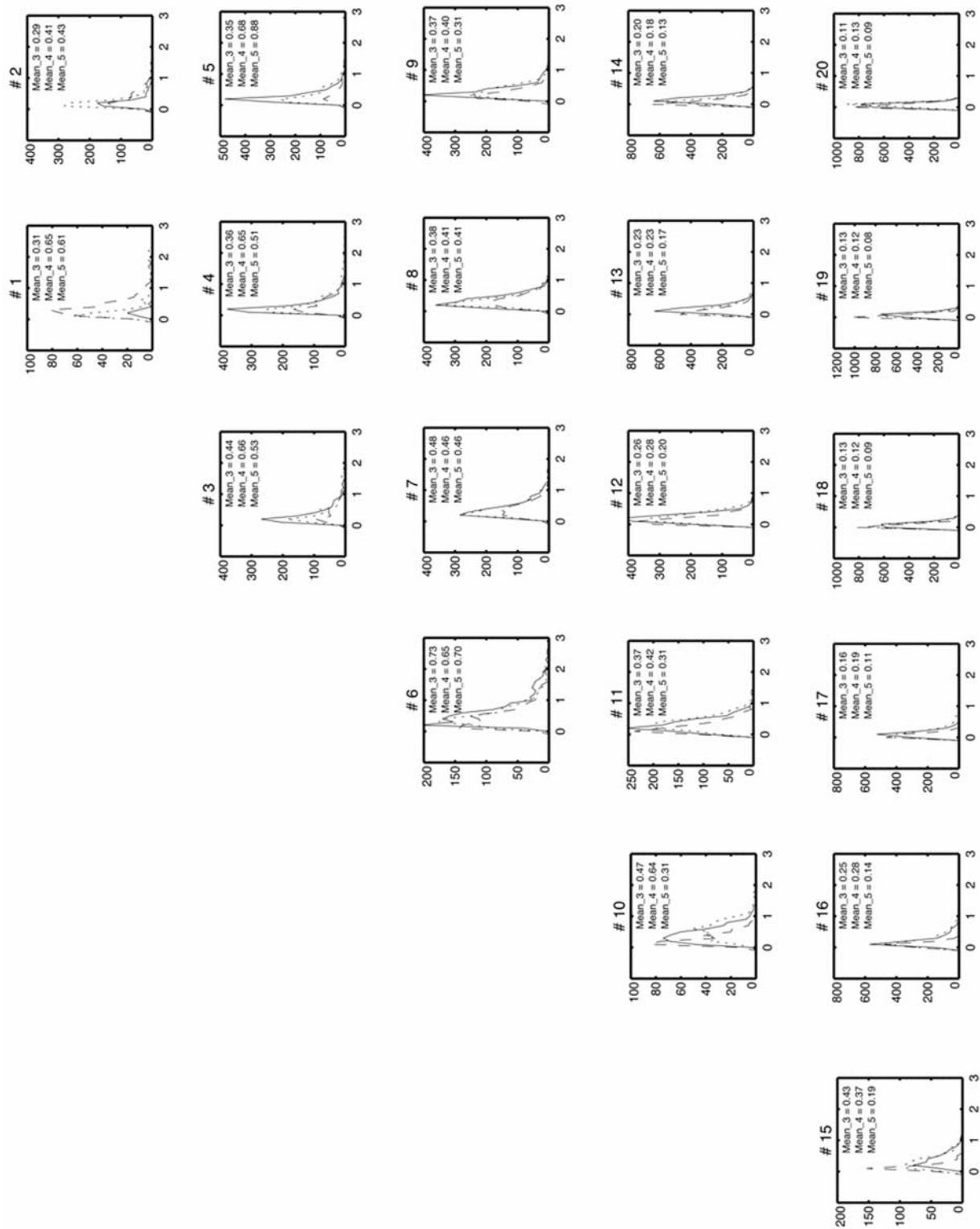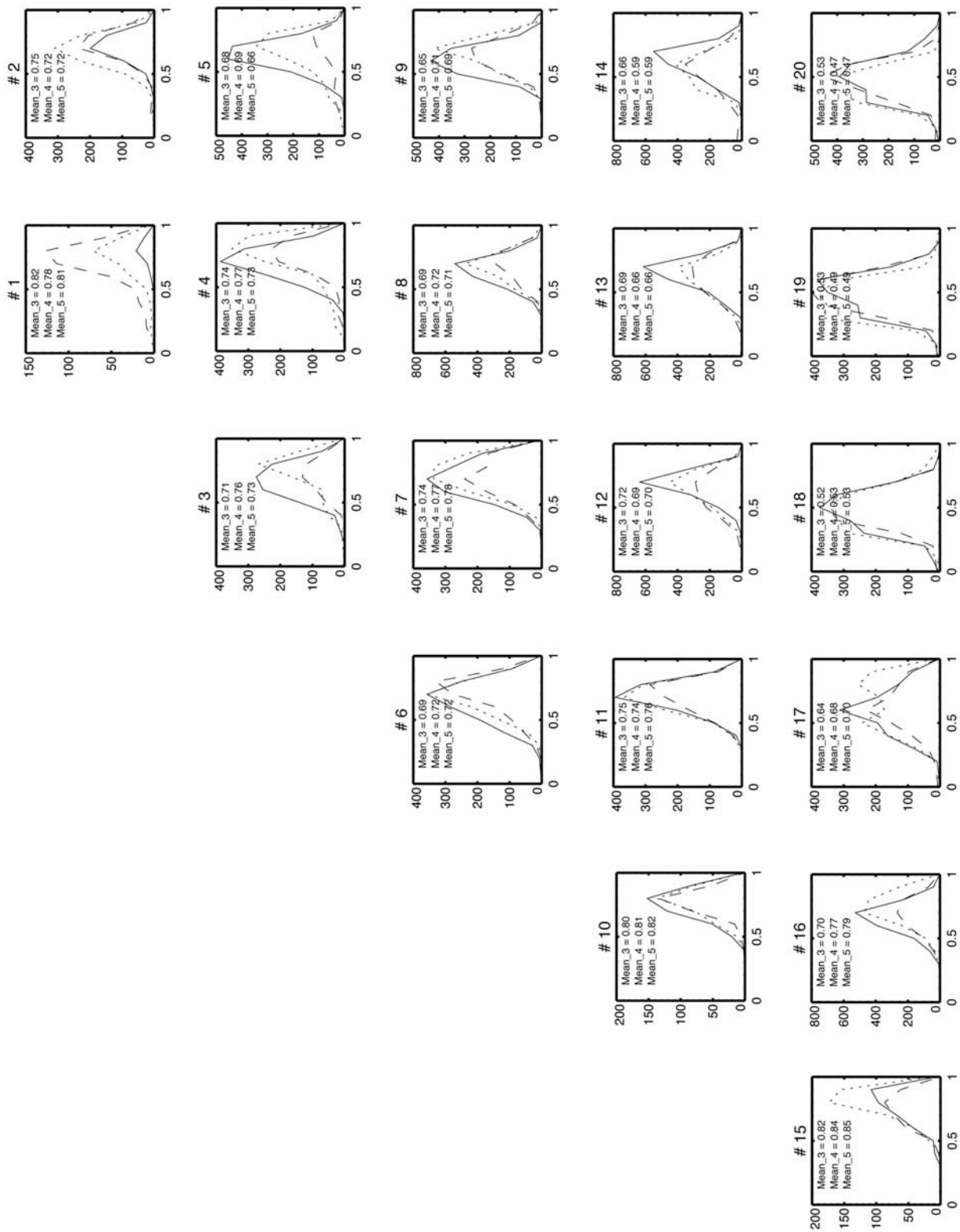**Figure 5a.** Histograms of regional monthly $\tau_a$ in March, April, and May 2001.

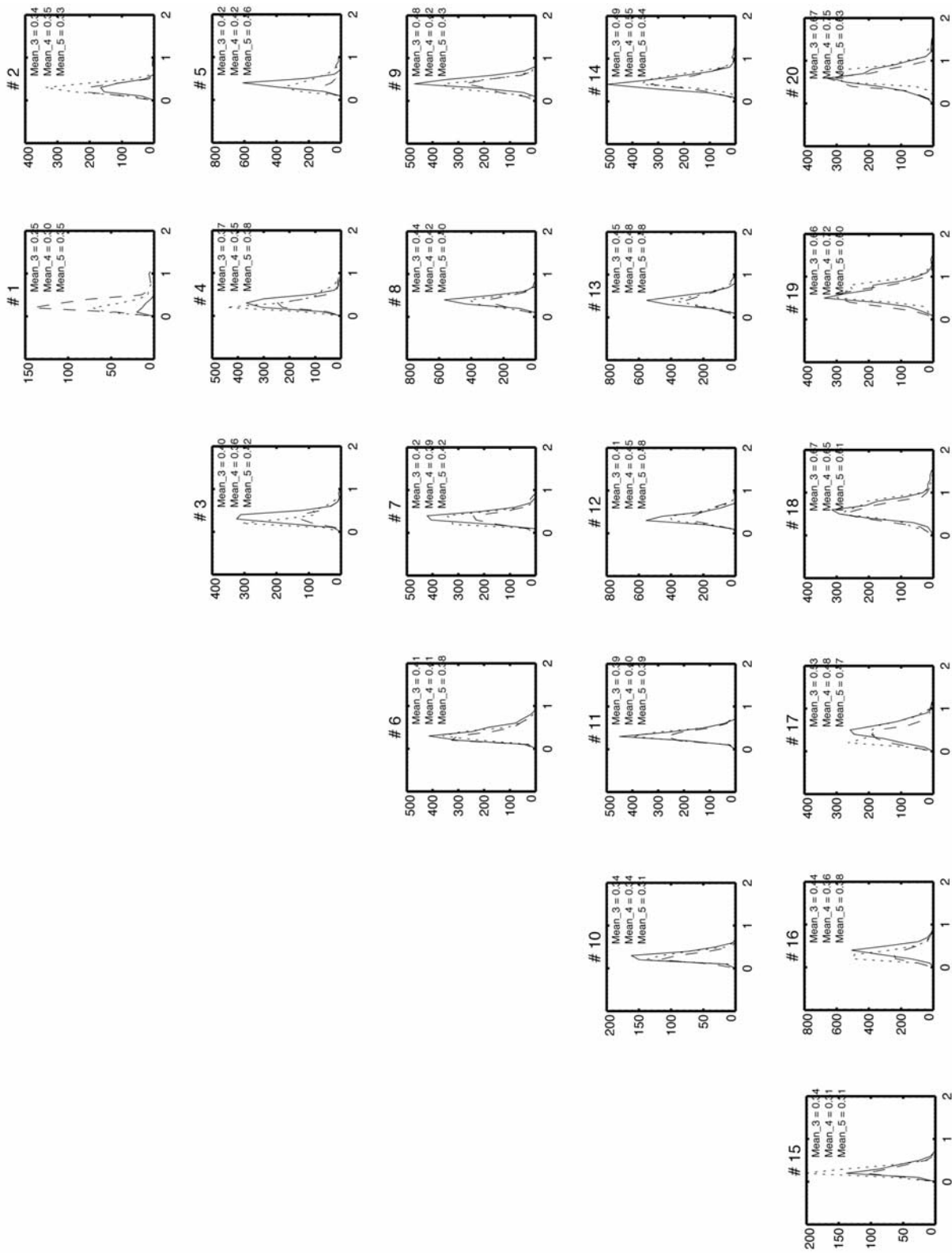**Figure 5b.** Same as in Figure 5a but for η in March, April, and May 2001.

**Figure 5c.** Same as in Figure 5a but for $r_{eff}r_{eff}$ in March, April, and May 2001.

**Table 1.** Monthly Mean and Median Aerosol Optical Depth Derived in 20 Regions in March, April, and May 2001[a]

| Region | March Mean(SD), Median | April Mean(SD), Median | May Mean(SD), Median |
|---|---|---|---|
| 1 | 0.31(0.24), 0.27 | 0.65(1.10), 0.24 | 0.61(0.74), 0.38 |
| 2 | 0.29(0.20), 0.24 | 0.41(0.57), 0.25 | 0.43(0.40), 0.32 |
| 3 | 0.44(0.42), 0.32 | 0.66(0.80), 0.37 | 0.53(0.51), 0.43 |
| 4 | 0.39(0.33), 0.27 | 0.65(0.88), 0.34 | 0.51(0.63), 0.36 |
| 5 | 0.35(0.30), 0.28 | 0.68(0.96), 0.36 | 0.88(1.16), 0.39 |
| 6 | 0.73(0.63), 0.55 | 0.65(0.58), 0.49 | 0.70(0.76), 0.50 |
| 7 | 0.48(0.33), 0.38 | 0.46(0.25), 0.39 | 0.46(0.30), 0.41 |
| 8 | 0.38(0.19), 0.35 | 0.41(0.22), 0.36 | 0.41(0.29), 0.37 |
| 9 | 0.37(0.25), 0.31 | 0.40(0.23), 0.37 | 0.31(0.21), 0.27 |
| 10 | 0.47(0.32), 0.42 | 0.64(0.33), 0.61 | 0.31(0.19), 0.25 |
| 11 | 0.37(0.24), 0.32 | 0.42(0.23), 0.38 | 0.31(0.29), 0.24 |
| 12 | 0.26(0.15), 0.24 | 0.28(0.17), 0.25 | 0.20(0.16), 0.17 |
| 13 | 0.23(0.12), 0.20 | 0.23(0.16), 0.19 | 0.17(0.16), 0.12 |
| 14 | 0.20(0.10), 0.19 | 0.18(0.12), 0.14 | 0.13(0.15), 0.09 |
| 15 | 0.43(0.23), 0.39 | 0.37(0.24), 0.33 | 0.19(0.11), 0.16 |
| 16 | 0.25(0.16), 0.19 | 0.28(0.31), 0.21 | 0.14(0.07), 0.13 |
| 17 | 0.16(0.09), 0.14 | 0.19(0.16), 0.15 | 0.11(0.07), 0.09 |
| 18 | 0.13(0.07), 0.11 | 0.12(0.09), 0.10 | 0.09(0.05), 0.08 |
| 19 | 0.13(0.06), 0.12 | 0.12(0.06), 0.10 | 0.08(0.05), 0.07 |
| 20 | 0.11(0.06), 0.10 | 0.13(0.05), 0.12 | 0.09(0.06), 0.08 |

[a]SD, standard deviation.

**Table 3.** Monthly Mean, Standard Deviation, and Median of Effective Radius Derived in 20 Regions in March, April, and May 2001[a]

| Region | March Mean(SD), Median | April Mean(SD), Median | May Mean(SD), Median |
|---|---|---|---|
| 1 | 0.25(0.09), 0.28 | 0.30(0.16), 0.28 | 0.35(0.18), 0.32 |
| 2 | 0.34(0.10), 0.34 | 0.35(0.11), 0.34 | 0.33(0.16), 0.32 |
| 3 | 0.40(0.13), 0.39 | 0.36(0.16), 0.32 | 0.42(0.17), 0.40 |
| 4 | 0.37(0.12), 0.39 | 0.35(0.16), 0.30 | 0.38(0.19), 0.34 |
| 5 | 0.37(0.12), 0.36 | 0.42(0.15), 0.39 | 0.46(0.24), 0.37 |
| 6 | 0.41(0.15), 0.38 | 0.41(0.14), 0.38 | 0.38(0.16), 0.34 |
| 7 | 0.42(0.12), 0.41 | 0.39(0.12), 0.39 | 0.42(0.15), 0.40 |
| 8 | 0.44(0.10), 0.48 | 0.42(0.11), 0.41 | 0.40(0.12), 0.40 |
| 9 | 0.48(0.11), 0.48 | 0.42(0.11), 0.41 | 0.43(0.14), 0.48 |
| 10 | 0.34(0.10), 0.34 | 0.34(0.09), 0.32 | 0.31(0.09), 0.30 |
| 11 | 0.39(0.11), 0.38 | 0.40(0.11), 0.38 | 0.39(0.14), 0.36 |
| 12 | 0.41(0.11), 0.40 | 0.45(0.14), 0.42 | 0.48(0.18), 0.46 |
| 13 | 0.45(0.12), 0.44 | 0.48(0.14), 0.46 | 0.48(0.20), 0.44 |
| 14 | 0.49(0.14), 0.47 | 0.55(0.14), 0.58 | 0.54(0.23), 0.50 |
| 15 | 0.34(0.12), 0.31 | 0.31(0.10), 0.29 | 0.31(0.11), 0.30 |
| 16 | 0.44(0.12), 0.44 | 0.36(0.13), 0.34 | 0.38(0.17), 0.36 |
| 17 | 0.53(0.19), 0.52 | 0.48(0.22), 0.45 | 0.47(0.24), 0.45 |
| 18 | 0.67(0.22), 0.64 | 0.65(0.22), 0.64 | 0.61(0.21), 0.58 |
| 19 | 0.66(0.22), 0.68 | 0.72(0.21), 0.70 | 0.60(0.20), 0.59 |
| 20 | 0.67(0.23), 0.65 | 0.75(0.20), 0.78 | 0.63(0.21), 0.61 |

[a]SD, standard deviation.

Express" can move dust-laden air across the Pacific Ocean within 4–10 days. Figure 2 depicts NASA GMAO (Global Modeling and Assimilation Office, formerly known as Data Assimilation Office) assimilated monthly mean wind fields (at 700 and 850 mb levels) for March, April, and May 2001. Similar patterns are found at both levels except the winds are much stronger and more organized at 700 mb than 850 mb. The winds also appear to be stronger and more organized in March and April as compared to May. As pointed out by *Chou et al.* [2002] that atmospheric circulation has strong influence on oceanic aerosol distribution, the largest $\tau_a$ values averaged over 100° and 160°E from level 3 1° × 1° daily aerosol products (ocean

**Table 2.** Mean, Standard Deviation, and Median of Fine-Mode Fraction Derived in 20 Regions in March, April, and May 2001[a]

| Region | March Mean(SD), Median | April Mean(SD), Median | May Mean(SD), Median |
|---|---|---|---|
| 1 | 0.82(0.11), 0.84 | 0.78(0.17), 0.82 | 0.75(0.16), 0.79 |
| 2 | 0.75(0.10), 0.76 | 0.72(0.12), 0.74 | 0.76(0.14), 0.77 |
| 3 | 0.71(0.13), 0.72 | 0.76(0.17), 0.80 | 0.74(0.14), 0.75 |
| 4 | 0.74(0.12), 0.75 | 0.77(0.18), 0.81 | 0.78(0.16), 0.80 |
| 5 | 0.68(0.11), 0.68 | 0.69(0.16), 0.72 | 0.66(0.19), 0.71 |
| 6 | 0.69(0.15), 0.71 | 0.72(0.13), 0.74 | 0.74(0.15), 0.77 |
| 7 | 0.74(0.14), 0.74 | 0.77(0.13), 0.78 | 0.75(0.14), 0.76 |
| 8 | 0.69(0.11), 0.70 | 0.72(0.11), 0.73 | 0.73(0.12), 0.74 |
| 9 | 0.65(0.10), 0.65 | 0.71(0.11), 0.73 | 0.69(0.13), 0.70 |
| 10 | 0.80(0.11), 0.81 | 0.81(0.11), 0.83 | 0.81(0.10), 0.83 |
| 11 | 0.75(0.11), 0.76 | 0.74(0.12), 0.75 | 0.75(0.13), 0.77 |
| 12 | 0.72(0.11), 0.74 | 0.69(0.13), 0.71 | 0.66(0.15), 0.67 |
| 13 | 0.69(0.11), 0.70 | 0.66(0.13), 0.68 | 0.65(0.16), 0.67 |
| 14 | 0.66(0.12), 0.68 | 0.59(0.12), 0.60 | 0.58(0.17), 0.61 |
| 15 | 0.82(0.13), 0.83 | 0.84(0.12), 0.86 | 0.79(0.12), 0.80 |
| 16 | 0.70(0.11), 0.71 | 0.77(0.13), 0.78 | 0.73(0.13), 0.74 |
| 17 | 0.64(0.17), 0.64 | 0.68(0.20), 0.70 | 0.66(0.18), 0.66 |
| 18 | 0.52(0.15), 0.54 | 0.53(0.15), 0.52 | 0.54(0.14), 0.55 |
| 19 | 0.53(0.15), 0.55 | 0.49(0.14), 0.49 | 0.54(0.14), 0.55 |
| 20 | 0.53(0.15), 0.54 | 0.47(0.12), 0.48 | 0.52(0.14), 0.54 |

[a]SD, standard deviation.

only) are found in 30°–40°N in March (~0.48) and 40°–50°N in April (~0.51) (see Figure 3), coinciding with the maximum wind speed of prevailing westerly as shown in Figure 2.

[11] To illustrate the spatial variability of aerosol loading and size in terms of distance from emission sources, we further divide the domain (10°–60°N and 100°–160°E) of ACE-Asia into twenty 10° × 10° regions (see Figure 4). In each (10° × 10°) region, we calculate the monthly mean, standard deviation, and median of $\tau_a$, $\eta$, and $r_{eff}$ for March, April, and May 2001 (see Tables 1–3). The monthly histograms (derived with level 3 daily products) are also shown in Figures 5a, 5b, and 5c for comparing $\tau_a$, $\eta$, and $r_{eff}$ distribution in each region. It is found in general that the farther away from the land, the smaller aerosol loading is. As expected, higher monthly mean $\tau_a$ (>0.3) and larger variation of the mean values (e.g., standard deviation) are clearly seen in regions 1, 2, 3, 4, 6, and 7 (primarily dust and pollution), 10 and 11 (primarily pollution and smoke), and 15 (primarily smoke) near the Asian continent associated with dust, pollution, and biomass-burning emission sources. The large standard deviation found with high aerosol loading can be translated into large difference between monthly mean and median values (see Table 1), for example, up to 0.4 in regions 1–6 as attributed to more frequent dust outbreaks in April as opposed to 0.2 in March and May. However, it is not always the case. In region 5 (remote ocean), for example, the monthly mean $\tau_a$ ~0.88 with difference ~0.49 in May, which cannot be explained by either dust emission or long-range transport, is most likely attributed to residual cloud contamination. In contrast to the impact mostly from dust outbreaks at the north of 30°N, Southeast Asia biomass burning shows large influence at the south of 30°N in March and April, and a noticeable decrease in May signaling diminishing agricultural burns before the onset of Monsoon season.

**Table 4.** Spectral Aerosol Optical Depths Derived by MODIS and AATS on Board C-130 and Twin Otter[a]

| | 0.47 μm | 0.55 μm | 0.66 μm | 0.86 μm | 1.24 μm | 1.64 μm | 2.13 μm |
|---|---|---|---|---|---|---|---|
| *6 April 2001 (32.9°N, 127.2°E;UTC(MODIS) 0200;UTC(AATS-14) 0150, SRMSE = 0.015,42 m asl)* | | | | | | | |
| MODIS(O) | 0.43 ± 0.07 | 0.36 ± 0.06 | 0.30 ± 0.05 | 0.22 ± 0.04 | 0.15 ± 0.03 | 0.11 ± 0.02 | 0.09 ± 0.02 |
| AATS-14 | 0.41 ± 0.008 | 0.35 ± 0.007 | 0.28 ± 0.006 | 0.22 ± 0.004 | 0.16 ± 0.003 | 0.13 ± 0.003 | |
| *8 April 2001 (34.1°N, 132.2°E;UTC(MODIS) 0150;UTC(AATS-6) 0210, SRMSE = 0.072, 17 m asl)* | | | | | | | |
| MODIS(L) | 0.54 ± 0.05 | 0.43 ± 0.05 | 0.32 ± 0.05 | | | | |
| AATS-6 | 0.45 ± 0.007 | 0.36 ± 0.006 | 0.27 ± 0.004 | 0.19 ± 0.002 | | | |
| *8 April 2001 (34.2°N, 132.2°E;UTC(MODIS) 0145;UTC(AATS-14) 0220, SRMSE = 0.067, 6 m asl)* | | | | | | | |
| MODIS(L) | 0.54 ± 0.05 | 0.43 ± 0.05 | 0.32 ± 0.05 | | | | |
| AATS-14 | 0.45 ± 0.005 | 0.37 ± 0.02 | 0.28 ± 0.02 | 0.25 ± 0.02 | 0.22 ± 0.02 | 0.21 ± 0.02 | |
| *12 April 2001 (33.1°N, 127.5°E;UTC(MODIS) 0300;UTC(AATS-14)0320, SRMSE = 0.11, 13 m asl)* | | | | | | | |
| MODIS(O) | 0.49 ± 0.01 | 0.44 ± 0.01 | 0.40 ± 0.01 | 0.34 ± 0.01 | 0.29 ± 0.01 | 0.26 ± 0.01 | 0.24 ± 0.009 |
| AATS-14 | 0.33 ± 0.02 | 0.30 ± 0.02 | 0.28 ± 0.02 | 0.25 ± 0.02 | 0.22 ± 0.02 | 0.21 ± 0.02 | |
| *13 April 2001 (35.8°N, 132.4°E;UTC(MODIS) 0205;UTC(AATS-6) 0155, SRMSE = 0.015, 43 m asl)* | | | | | | | |
| MODIS(O) | 0.30 ± 0.01 | 0.25 ± 0.01 | 0.21 ± 0.01 | 0.15 ± 0.007 | 0.11 ± 0.006 | 0.10 ± 0.005 | 0.009 ± 0.005 |
| AATS-6 | 0.29 ± 0.01 | 0.23 ± 0.01 | 0.19 ± 0.01 | 0.15 ± 0.008 | | | |
| *14 April 2001 (32.3°N, 132.5°E;UTC(MODIS) 0250;UTC(AATS-14) 0310, SRMSE = 0.3, 34 m asl)* | | | | | | | |
| MODIS(O) | 1.23 ± 0.19 | 1.10 ± 0.18 | 1.00 ± 0.17 | 0.86 ± 0.16 | 0.76 ± 0.13 | 0.70 ± 0.10 | 0.63 ± 0.08 |
| AATS-14 | 0.77 ± 0.03 | 0.73 ± 0.02 | 0.68 ± 0.02 | 0.63 ± 0.02 | 0.58 ± 0.02 | 0.56 ± 0.01 | |
| *19 April 2001 (37.2°N, 133.4°E;UTC(MODIS) 0130;UTC(AATS-14) 0140, SRMSE = 0.04, 41 m asl)* | | | | | | | |
| MODIS(O) | 0.49 ± 0.01 | 0.40 ± 0.01 | 0.33 ± 0.007 | 0.23 ± 0.005 | 0.15 ± 0.003 | 0.11 ± 0.003 | 0.084 ± 0.003 |
| AATS-14 | 0.43 ± 0.02 | 0.37 ± 0.02 | 0.30 ± 0.01 | 0.25 ± 0.01 | 0.19 ± 0.007 | 0.16 ± 0.006 | |
| *20 April 2001 (35.0°N, 140.6°E;UTC(MODIS) 0210;UTC(AATS-6) 0215, SRMSE = 0.02, 33 m asl)* | | | | | | | |
| MODIS(O) | 0.39 ± 0.03 | 0.32 ± 0.02 | 0.27 ± 0.01 | 0.19 ± 0.01 | 0.13 ± 0.01 | 0.11 ± 0.01 | 0.009 ± 0.001 |
| AATS-6 | 0.43 ± 0.008 | 0.31 ± 0.01 | 0.25 ± 0.007 | 0.18 ± 0.005 | | | |
| *23 April 2001 (32.4°N, 139.6°E;UTC(MODIS) 0105;UTC(AATS-6) 0120, SRMSE = 0.012, 30 m asl)* | | | | | | | |
| MODIS(O) | 0.33 ± 0.008 | 0.28 ± 0.007 | 0.24 ± 0.007 | 0.17 ± 0.005 | 0.12 ± 0.004 | 0.10 ± 0.01 | 0.009 ± 0.003 |
| AATS-6 | 0.33 ± 0.02 | 0.27 ± 0.02 | 0.23 ± 0.02 | 0.19 ± 0.01 | | | |
| *23 April 2001 (33.1°N, 134.1°E;UTC(MODIS) 0245;UTC(AATS-14) 0306, SRMSE = 0.026, 20 m asl)* | | | | | | | |
| MODIS(O) | 0.31 ± 0.03 | 0.27 ± 0.03 | 0.23 ± 0.02 | 0.18 ± 0.02 | 0.14 ± 0.02 | 0.12 ± 0.02 | 0.10 ± 0.02 |
| AATS-14 | 0.28 ± 0.009 | 0.25 ± 0.008 | 0.22 ± 0.006 | 0.19 ± 0.005 | 0.17 ± 0.004 | 0.16 ± 0.003 | |
| *2 May2001 (33.2°N, 126.1°E;UTC(MODIS) 0235;UTC(AATS-6) 0240, SRMSE = 0.093, 30 m asl)* | | | | | | | |
| MODIS(L) | 0.59 ± 0.04 | 0.44 ± 0.06 | 0.32 ± 0.07 | | | | |
| AATS-6 | 0.45 ± 0.06 | 0.37 ± 0.05 | 0.28 ± 0.04 | 0.19 ± 0.03 | | | |

[a]Aerosol optical depths are given as mean ± standard deviation. Abbreviations are as follows: L, land; O, ocean; asl, above sea level; SRMSE, cross-spectrum root mean square error. GPS altitudes are used for AATS instruments.

[12] The monthly mean η of 0.65−0.85 are generally found in most of the regions except in regions 18−20 (remote ocean) with η ranging from 0.45 to 0.55. Standard deviations are shown in the range between 0.1 and 0.2 regardless of the locations. It is reasonable that wider range of η is seen in low latitudes (50°−60°N: 0.70−0.85; 30°−50°N: 0.65−0.8; 20°−30°: 0.55−0.85; 10−20°N: 0.45−0.85) as aerosol loading is increasingly influenced by sea salt. However, only small regional monthly mean differences (≤0.05), and small differences between regional monthly mean and median values (≤0.05) are found in η unlike. There also appears to be no noticeable change in η in responding to the change in $\tau_a$. It is therefore difficult to distinguish the differences between the monthly mean η of the range of 0.7−0.8 in the dust frequently affected regions (i.e., 3, 4, 6, and 7) and 0.8−0.85 in regions (10 and 15) largely influenced by biomass burning smoke.

[13] The regional monthly mean $r_{eff}$ derived are generally confined to a range within 0 to 1 μm with standard deviation ranging from 0.1 to 0.25 μm, except for limited number of values > 1 μm in region 5 and regions 18−20 as discussed earlier. Similar to η, the differences between regional monthly mean and median are also small (<0.05−0.1 μm). Also like η, the regional monthly mean $r_{eff}$ show latitudinal variation (50°−60°N: 0.25−0.35 μm; 40°−50°N: 0.35−0.45 μm; 30°−40°N: 0.4−0.45 μm; 20°−30°N: 0.35−0.55 μm; 10−20°N: 0.3−0.75 μm). Given the η values of 0.7−0.8 in regions 3, 4, 6, and 7 (possibly mixed by dust and pollution aerosols) as shown above, $r_{eff}$ values are found in the range of 0.35−0.45 μm, and given the fine-mode fraction of 0.8−0.85 in regions 10 and 15 (smoke and pollution), $r_{eff}$ are in the range between 0.3 and 0.4 μm. Though the former, to some extent, may be underestimated by the assumption of spherical dust particle, the differences are still unexpectedly small.

## 4. Aerosol Optical Depth

[14] During ACE-Asia airborne and shipborne Sun photometers provide valuable aerosol information over open
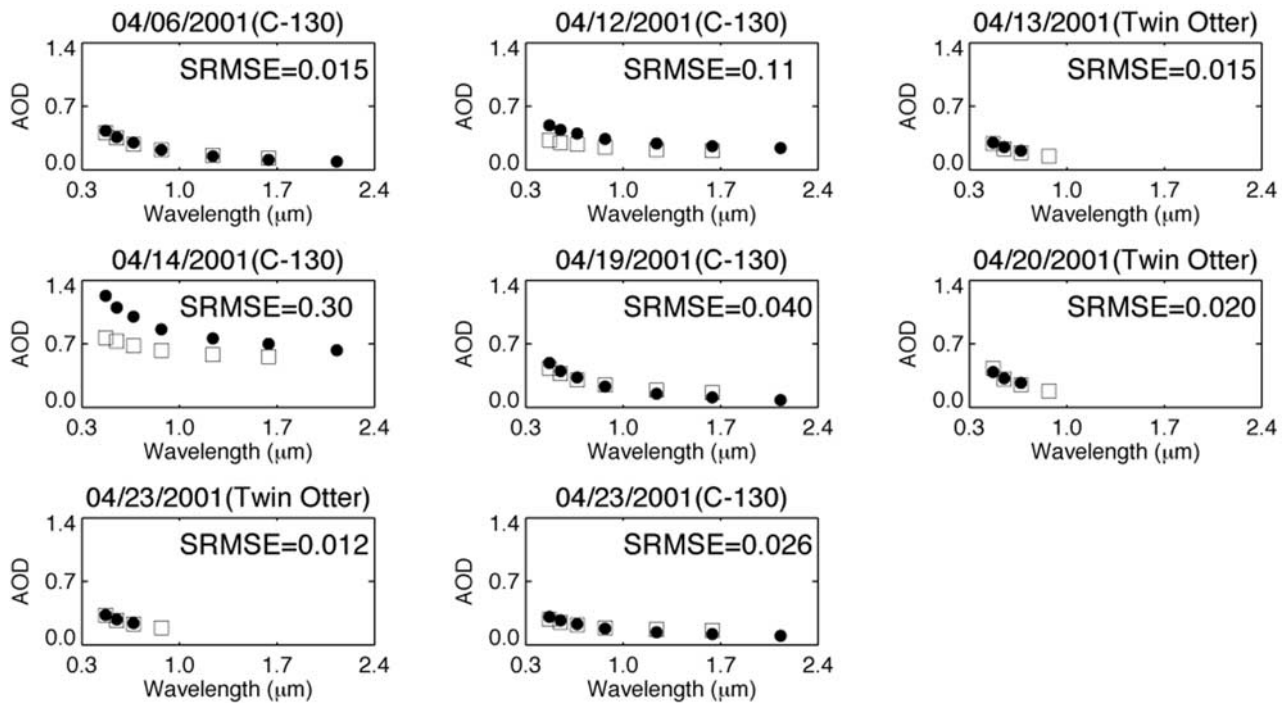
**Figure 6.** MODIS (circles) and airborne C-130/Twin Otter AATS (squares) derived $\tau_a$ values at 0.47, 0.55, 0.67, 1.24, 1.64, and 2.1 μm wavelengths.

oceans. The validation presented here involves all Sun photometers (Ames Airborne Tracking Sun photometer, Microtops, Simbad, and SimbadA) and radiometer (Multi-filter Rotating Shadowband Radiometer) on board various platforms (i.e., the C-130 airplane, the Twin-Otter airplane, and R/V *Ron Brown*).

## 4.1. MODIS Versus AATS on Board C-130 and Twin Otter

[15] The AATS-6 Sun photometer (6 channels: 0.380, 0.451, 0.525, 0.864, 0.941, and 1.021 μm) [*Matsumoto et al.*, 1987] on board the C-130 and AATS-14 (14 channels: 0.354, 0.38, 0.449, 0.454, 0.500, 0.525, 0.606, 0.675, 0.779, 0.864, 0.940, 1.019, 1.240, and 1.558 μm) on board the Twin Otter provide aerosol extinction measurements, which can be used to validate MODIS $\tau_a$ retrievals. The airborne Sun photometer functions similarly to ground-based Sun photometers except they require more complicated and sensitive mechanism to track the Sun while in flight. The AATS-14 aerosol optical depths at wavelengths greater than 1 μm are especially valuable because of the rareness of these measurements. When measuring aerosol optical depth from airplanes for satellite validation, the flight altitude poses a potential problem. In principle, the lowest flight altitude would be most ideal for the columnar $\tau_a$ comparisons. In our study, we choose 50 m to be the maximum altitude allowed, which is a compromise between the number of measurements available at colocated space and time and errors permissible for validation purpose. At 50 m altitude, the error of $\tau_a$ is estimated to be ∼0.015 (at 0.55 μm), which is close to the MODIS retrieval limitation given the instrument calibration accuracy no better than 1%. It is worth noting that similar criteria shown here were used by *Kahn et*

*al.* [2004] for comparing with MISR (Multiangle Imaging Spectroradiometer) retrievals.

[16] A total of 11 cases meet the criteria of AATS (GPS) flight altitudes ≤ 50 m, in addition to ±30 minutes of MODIS overpass times and MODIS retrievals within ±0.25° (latitude and longitude) of the average location of AATS flight altitude ≤ 50 m. Table 4 tabulates MODIS and AATS spectral $\tau_a$ mean and standard deviation values, along with latitude, longitude, UTC time, flight altitude, and SRMSE (cross-spectrum root mean square error). Note that the AATS-6 and AATS-14 $\tau_a$ values are derived at exact MODIS wavelengths using the coefficients from a second-order polynomial fit provided by the AATS team for the ACE-Asia experiment (http://geo.arc.nasa.gov/sgg/AATS-website).

[17] Figure 6 shows the comparisons between MODIS-and AATS-derived $\tau_a$ values from 0.47 to 0.86 μm (AATS-6) and from 0.47 to 1.64 μm (AATS-14) at different locations over ocean. Good agreement is found between MODIS and AATS over ocean with SRMSE < 0.05, except in case 2 (SRMSE ∼0.11) and 4 (SRMSE ∼0.3). The elevated AATS $\tau_a$ shown in SWIR spectrum (1.24 and 1.64 μm) in both cases (2 and 4) indicates the existence of dust particles and that dust nonsphericity could play a role in MODIS' overestimation of $\tau_a$. Because of the exclusion of sunglint (glint angle ≤ 40°) in MODIS aerosol retrieval, only two groups of scattering angles (110°–115° and 145°–155°) were derived. Given the largest spherical and non-spherical (e.g., spheroid) phase function differences between 110° and 130° (spheroid phase function > spherical phase function) [*Mishchenko et al.*, 1997], the use of spheroid phase function would produce more comparable MODIS $\tau_a$ retrievals with AATS measurements. For cases
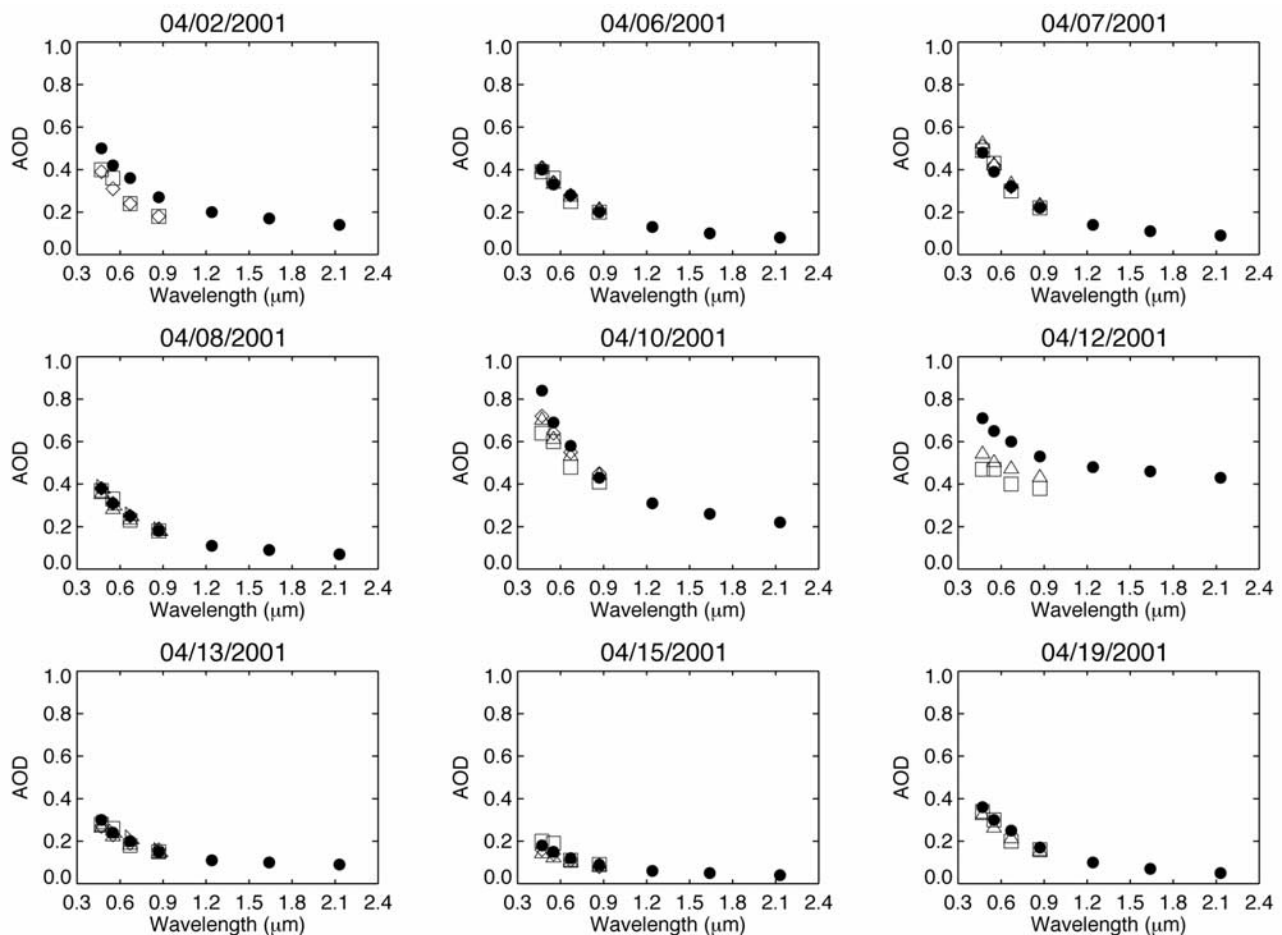
**Figure 7.** MODIS (circles) and R/V *Ron Brown* shipborne radiometers/Sun photometer derived $\tau_a$ values at 0.47, 0.55, 0.67, 1.24, 1.64, and 2.1 $\mu$m wavelengths. Different open symbols represent different shipborne Sun photometers/radiometers (squares, MFRSR; diamonds, MTPS; equilateral triangles, SBAD; and right triangles, SBADA).

1, 5, and 8 with SRMSE $\leq$ 0.04, the MODIS-derived $\tau_a$ shows slightly larger values for $\lambda < 1$ $\mu$m and slightly smaller values for $\lambda > 1$ $\mu$m when compared to AATS-14 results (cf. Figure 6), for which uncertainty in size distribution or spectral curvature of MODIS measurements is suspected to play a role.

## 4.2. MODIS Versus Sun Photometer/Radiometers on Board R/V *Ronald Brown*

[18] Four types of Sun photometers/radiometers (Microtops II Sun photometer, MTSP; Simbad, SBAD; SimbadA, SBADA; Multifilter Rotating Shadowband Radiometer, MFRSR) were operated on board the NOAA R/V *Ron Brown* over the western Pacific Ocean during ACE-Asia. MTPS is configured with 5 spectral channels (0.38, 0.44, 0.50, 0.675, and 0.87 $\mu$m) with a field of view of 2.5°. The handheld MTPS needs to operate manually. Simbad (0.443, 0.49, 0.565, 0.67, and 0.87 $\mu$m) and SimbadA (Advanced version of Simbad; 0.35, 0.38, 0.412, 0.443, 0.49, 0.51, 0.56, 0.62, 0.67, and 0.75 $\mu$m) are designed by LOA (Laboratoire d'Optique Atmospherique, France) with 10 nm bandwidth and 3° field-of-view to validate ocean color. They can also be used to measure aerosol optical depth by aiming at the Sun. Both require manual operations. MFRSR has six narrow bands (10 nm bandwidth) centered at 0.415, 0.499, 0.614, 0.67, 0.868, 0.936 and a broadband covering the entire solar spectrum. MFRSR is designed to automatically measure diffusive solar radiation at a 30-s interval. The difference between the two measurements represents the direct beam. The direct-beam calibration constants were differed by less than 1% between these two calibrations, corresponding to an uncertainty of ~0.01 aerosol optical depth (or less with lower solar elevation). The calibrations of these instruments were done using a Langley plot approach [*Shaw*, 1983] prior to the cruise by the manufacturer and again at Mauna Loa after the cruise [*Knobelspiesse et al.*, 2003; *Deschamps et al.*, 2004; *Miller et al.*, 2001].

[19] Table 5 tabulates aerosol optical depths derived by MODIS, MTPS, MFRSR, SBAD, and SBADA. For direct comparison, aerosol optical depths from MTPS, MFRSR, SBAD, and SBADA are interpolated to MODIS spectral channel wavelengths using the values at the two nearest wavelengths and then averaged over ±30 minutes of MODIS overpass times. The MODIS $\tau_a$ values (averaged within ±0.25° box at the locations of R/V *Ron Brown*) are in

**Table 5.** Spectral Aerosol Optical Depths Derived by MODIS and Sun Photometers/Radiometers on Board NOAA R/V *Ronald Brown*[a]

| | 0.47 μm | 0.55 μm | 0.66 μm | 0.86 μm | 1.24 μm | 1.64 μm | 2.13 μm |
|---|---|---|---|---|---|---|---|
| *2 April 2001 (32.8°N, 136.6°E;UTC(MODIS) 0225;UTC(MFRSR) 0243;UTC(MTPS) 0238)* | | | | | | | |
| MODIS | 0.50 ± 0.03 | 0.42 ± 0.03 | 0.36 ± 0.02 | 0.27 ± 0.02 | 0.20 ± 0.02 | 0.17 ± 0.02 | 0.14 ± 0.02 |
| MFRSR | 0.40 ± 0.03 | 0.36 ± 0.03 | 0.24 ± 0.02 | 0.18 ± 0.01 | (SRMSE = 0.095) | | |
| MTPS | 0.39 ± 0.004 | 0.31 ± 0.03 | 0.24 ± 0.004 | 0.18 ± 0.002 | (SRMSE = 0.097) | | |
| | | | | | | | |
| *6 April 2001 (32.9°N, 127.8°E;UTC(MODIS) 0200;UTC(MFRSR) 0149;UTC(MTPS) 0149; UTC(SBAD) 0159)* | | | | | | | |
| MODIS | 0.40 ± 0.04 | 0.33 ± 0.03 | 0.28 ± 0.03 | 0.20 ± 0.02 | 0.13 ± 0.02 | 0.10 ± 0.01 | 0.08 ± 0.01 |
| MFRSR | 0.39 ± 0.01 | 0.36 ± 0.01 | 0.25 ± 0.03 | 0.20 ± 0.005 | (SRMSE = 0.022) | | |
| MTPS | 0.41 ± 0.004 | 0.34 ± 0.01 | 0.28 ± 0.01 | 0.21 ± 0.007 | (SRMSE = 0.008) | | |
| SBAD | 0.40 ± 0.01 | 0.33 ± 0.01 | 0.27 ± 0.01 | 0.21 ± 0.004 | (SRMSE = 0.007) | | |
| SBADA | 0.40 ± 0.01 | 0.34 ± 0.01 | 0.28 ± 0.01 | 0.20 ± 0.005 | (SRMSE = 0.005) | | |
| | | | | | | | |
| *7 April 2001 (35.8°N, 132.4°E;UTC(MODIS) 0240;UTC(MFRSR) 0238;UTC(MTPS) 0218; UTC(SBAD) 0223)* | | | | | | | |
| MODIS | 0.48 ± 0.01 | 0.39 ± 0.01 | 0.32 ± 0.01 | 0.22 ± 0.01 | 0.14 ± 0.01 | 0.11 ± 0.01 | 0.09 ± 0.01 |
| MFRSR | 0.49 ± 0.02 | 0.43 ± 0.02 | 0.30 ± 0.01 | 0.22 ± 0.01 | (SRMSE = 0.023) | | |
| MTPS | 0.51 ± 0.003 | 0.42 ± 0.004 | 0.32 ± 0.004 | 0.23 ± 0.004 | (SRMSE = 0.022) | | |
| SBAD | 0.52 ± 0.02 | 0.42 ± 0.001 | 0.33 ± 0.01 | 0.23 ± 0.01 | (SRMSE = 0.026) | | |
| | | | | | | | |
| *8 April 2001 (38.0°N, 133.6°E;UTC(MODIS) 0145;UTC(MFRSR) 0146;UTC(MTPS) 0156; UTC(SBAD) 0146)* | | | | | | | |
| MODIS | 0.38 ± 0.01 | 0.31 ± 0.01 | 0.25 ± 0.02 | 0.18 ± 0.01 | 0.11 ± 0.005 | 0.09 ± 0.003 | 0.07 ± 0.003 |
| MFRSR | 0.37 ± 0.02 | 0.33 ± 0.02 | 0.23 ± 0.01 | 0.18 ± 0.01 | (SRMSE = 0.015) | | |
| MTPS | 0.38 ± 0.04 | 0.31 ± 0.03 | 0.25 ± 0.02 | 0.19 ± 0.02 | (SRMSE = 0.005) | | |
| SBAD | 0.35 ± 0.03 | 0.28 ± 0.02 | 0.23 ± 0.02 | 0.18 ± 0.01 | (SRMSE = 0.023) | | |
| SBADA | 0.38 ± 0.03 | 0.30 ± 0.03 | 0.25 ± 0.02 | 0.18 ± 0.02 | (SRMSE = 0.005) | | |
| | | | | | | | |
| *10 April 2001 (37.9°N, 130.8°E;UTC(MODIS) 0135;UTC(MFRSR) 0135;UTC(MTPS) 0127; UTC(SBAD) 0134)* | | | | | | | |
| MODIS | 0.84 ± 0.02 | 0.69 ± 0.02 | 0.58 ± 0.01 | 0.43 ± 0.01 | 0.31 ± 0.01 | 0.26 ± 0.01 | 0.22 ± 0.01 |
| MFRSR | 0.64 ± 0.01 | 0.60 ± 0.01 | 0.48 ± 0.01 | 0.41 ± 0.01 | (SRMSE = 0.12) | | |
| MTPS | 0.72 ± 0.001 | 0.64 ± 0.001 | 0.55 ± 0.001 | 0.45 ± 0.001 | (SRMSE = 0.067) | | |
| SBAD | 0.70 ± 0.01 | 0.61 ± 0.01 | 0.53 ± 0.01 | 0.44 ± 0.01 | (SRMSE = 0.085) | | |
| | | | | | | | |
| *12 April 2001 (35.0°N, 130.0°E;UTC(MODIS) 0300;UTC(MFRSR)0305; UTC(SMBD)0258)* | | | | | | | |
| MODIS | 0.71 ± 0.03 | 0.65 ± 0.03 | 0.60 ± 0.03 | 0.53 ± 0.03 | 0.48 ± 0.04 | 0.46 ± 0.04 | 0.43 ± 0.04 |
| MFRSR | 0.47 ± 0.02 | 0.47 ± 0.02 | 0.40 ± 0.02 | 0.38 ± 0.02 | (SRMSE = 0.195) | | |
| SBAD | 0.54 ± 0.02 | 0.50 ± 0.02 | 0.47 ± 0.02 | 0.43 ± 0.01 | (SRMSE = 0.139) | | |
| | | | | | | | |
| *13 April 2001 (35.7°N, 132.5°E;UTC(MODIS) 0205;UTC(MFRSR) 0204; UTC(MTPS) 0207;UTC(SBAD) 0206)* | | | | | | | |
| MODIS | 0.30 ± 0.01 | 0.24 ± 0.01 | 0.20 ± 0.01 | 0.15 ± 0.01 | 0.11 ± 0.005 | 0.10 ± 0.005 | 0.09 ± 0.005 |
| MFRSR | 0.28 ± 0.01 | 0.26 ± 0.01 | 0.18 ± 0.01 | 0.15 ± 0.01 | (SRMSE = 0.0173) | | |
| MTPS | 0.27 ± 0.01 | 0.23 ± 0.01 | 0.19 ± 0.01 | 0.16 ± 0.01 | (SRMSE = 0.0173) | | |
| SBAD | 0.26 ± 0.01 | 0.22 ± 0.01 | 0.18 ± 0.01 | 0.14 ± 0.01 | (SRMSE = 0.025) | | |
| SBADA | 0.28 ± 0.006 | 0.24 ± 0.005 | 0.21 ± 0.003 | 0.15 ± 0.003 | (SRMSE = 0.011) | | |
| | | | | | | | |
| *15 April 2001 (32.4°N, 128.5°E;UTC(MODIS) 0155;UTC(MFRSR) 0154; UTC(MTPS) 0159;UTC(SBAD) 0148)* | | | | | | | |
| MODIS | 0.18 ± 0.03 | 0.15 ± 0.03 | 0.12 ± 0.03 | 0.09 ± 0.02 | 0.06 ± 0.01 | 0.05 ± 0.01 | 0.04 ± 0.008 |
| MFRSR | 0.20 ± 0.01 | 0.19 ± 0.01 | 0.11 ± 0.01 | 0.09 ± 0.005 | (SRMSE = 0.0229) | | |
| MTPS | 0.16 ± 0.01 | 0.14 ± 0.01 | 0.11 ± 0.01 | 0.08 ± 0.007 | (SRMSE = 0.0132) | | |
| SBAD | 0.14 ± 0.01 | 0.12 ± 0.01 | 0.10 ± 0.01 | 0.08 ± 0.005 | (SRMSE = 0.0273) | | |
| | | | | | | | |
| *19 April 2001 (33.1°N, 135.2°E;UTC(MODIS) 0130;UTC(MFRSR) 0152; UTC(MTPS) 0159;UTC(SBAD) 0148)* | | | | | | | |
| MODIS | 0.36 ± 0.02 | 0.30 ± 0.01 | 0.25 ± 0.01 | 0.17 ± 0.01 | 0.10 ± 0.007 | 0.07 ± 0.006 | 0.05 ± 0.006 |
| MFRSR | 0.34 ± 0.01 | 0.30 ± 0.01 | 0.20 ± 0.01 | 0.16 ± 0.01 | (SRMSE = 0.0273) | | |
| SBAD | 0.32 ± 0.01 | 0.26 ± 0.01 | 0.21 ± 0.01 | 0.15 ± 0.01 | (SRMSE = 0.0361) | | |

[a]Aerosol optical depths are given as mean ± standard deviation. Abbreviations are as follows: MFRSR, Multifilter rotating shadowband radiometer; MTPS, microtops Sun photometer; SBAD, Simbad; SBADA, advanced Simbad; SRMSE, cross-spectrum root mean square error.

good agreement (SRMSE < 0.05) with Sun photometer/radiometers measurements except in case 5 (0.05–0.1), case 1 (SRMSE ∼0.1), and case 6 (SRMSE ∼0.1–0.2) (see Figure 7). The SRMSE values ∼0.1–0.2 in case 6 are consistent with that found previously between MODIS and AATS (∼0.1) that dust presence as seen by increased $\tau_a$ in SWIR band caused the large error. The cases with the range of errors between 0.05 and 0.1 are suspected to have a similar cause but of less dust abundance. Different instrument configuration and calibration of Sun photometers and shadowband radiometers may explain the differences of

SRMSE between them but the details are beyond the focus of this paper.

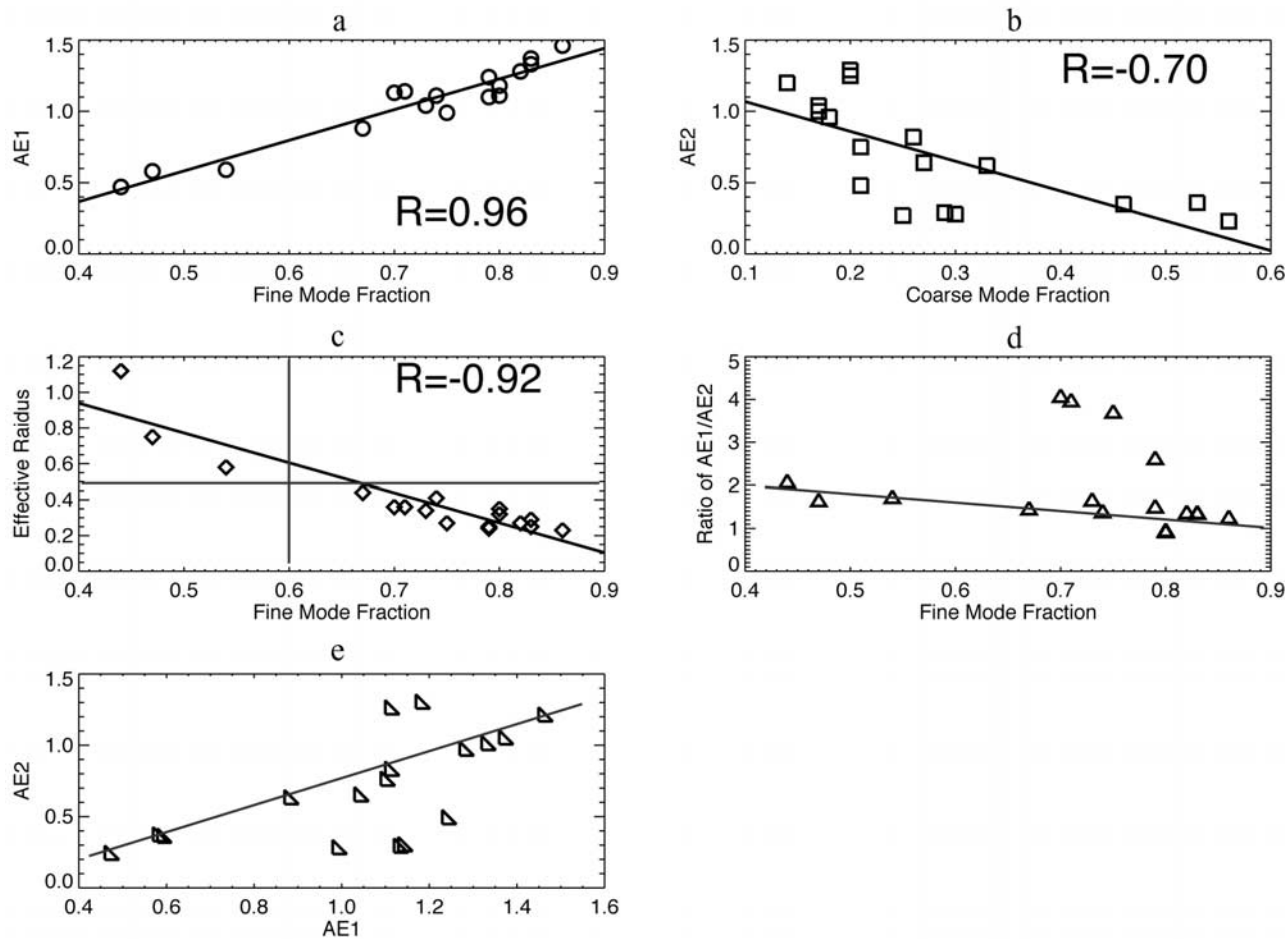## 5. Effective Radius and Fine-Mode Fraction

[20] We compare MODIS retrievals to AERONET inversions with both assuming aerosol particles in spherical shape. MODIS observes the total column ambient aerosol, similar to AERONET. Thus they are directly comparable. Here, however, we only focus on $r_{eff}$ and leave out the
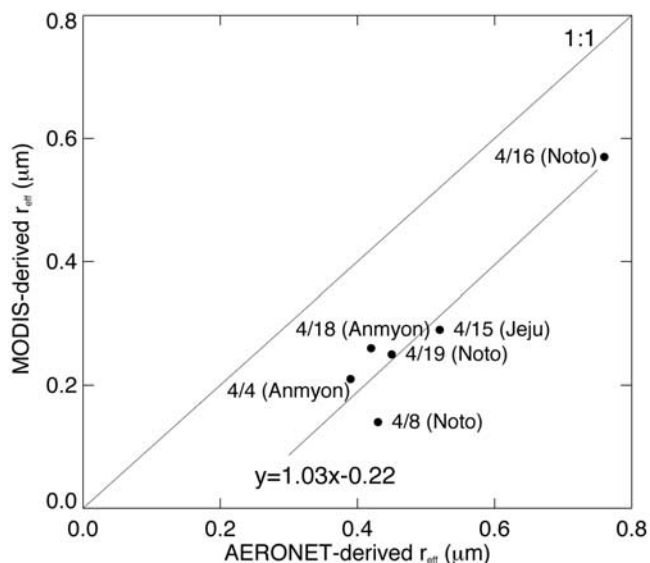
**Figure 8.** Comparison of MODIS- and AERONET-derived $r_{eff}$ in April 2001. The dates and the AERONET sites are shown for identification.

comparisons of η with AERONET to more comprehensive analysis as done by R. G. Kleidman et al. (personal communication, 2004), and as well the comparisons with in situ measurements led by T. R. Anderson et al. (personal communication, 2004). The former study points out that MODIS-derived η values are generally higher above 0.8 and lower below 0.6, and the latter shows that MODIS exaggerates even more during ACE-Asia period.

[21] The MODIS aerosol retrieval over ocean requires 100% clear water pixels within a $10 \times 10$ km$^2$, thus it excludes coasts and sediment-rich regions. Though a couple of MODIS validation results of $r_{eff}$ have been done [*Remer et al.*, 2002; *Levy et al.*, 2003] against the AERONET sky measurements [*Dubovik and King*, 2000], they are only suitable for conditions with homogeneous distribution of aerosol loading. Given a small number of AERONET island sites available to represent true oceanic conditions (less land contamination), since most AERONET sites (>90%) are situated inland and along the coasts, we have obtained only six pairs of MODIS- and AERONET-derived $r_{eff}$ from the process of collocating them in space (±50 km of AERONET site) and time (±1 hour of MODIS overpass) in April 2001. The AERONET sites with at least one coincidence (denoted



**Figure 9.** Relationship of MODIS-derived aerosol parameters (a) AE1 versus fine-mode fraction, (b) AE2 versus coarse-mode fraction, (c) effective radius versus fine-mode fraction, (d) ratio of AE1/AE2 versus fine-mode fraction, and (e) AE2 versus AE1.

**Table 6.** MODIS Aerosol Parameters of Mean (Standard Deviation) Over Ocean Collocated With AATS on Board C-130 and Twin, Shown in Boldface, and Sun Photometer/Radiometer on Board NOAA R/V *Ronald Brown*[a]

| $\tau_{0.55\,\mu m}$ | $\alpha_{0.66-0.86\mu m}$ | $\alpha_{0.86-2.13\,\mu m}$ | $r_{eff}$ | $\eta_{0.55\,\mu m}$ | $\Theta$ | $\psi_{0.55\,\mu m}$ | $\varepsilon$ | Modes (Fine, Coarse) |
|---|---|---|---|---|---|---|---|---|
| *2 April 2001 (32.8°N, 136.6°E; 0225 UTC)* | | | | | | | | |
| 0.42(0.03) | 1.04(0.06) | 0.64(0.03) | 0.34(0.02) | 0.73(0.02) | 111.3° | 0.72 | 1.93E-2 | (2,7.5) |
| *6 April 2001 (32.9°N, 127.8°E; 0200 UTC)* | | | | | | | | |
| 0.33(0.03) | 1.18(0.06) | 1.29(0.03) | 0.32(0.02) | 0.80(0.01) | 151.5° | 0.71 | 2.02E-2 | (3.5,8) |
| *6 April 2001 (32.9°N, 127.2°E; 0200 UTC)* | | | | | | | | |
| **0.36(0.06)** | **1.11(0.11)** | **1.25(0.15)** | **0.35(0.04)** | **0.80(0.01)** | **151.1°** | **0.70** | **1.47E-2** | **(3.3,8)** |
| *7 April 2001 (35.8°N, 132.4°E; 0240 UTC)* | | | | | | | | |
| 0.39(0.01) | 1.28(0.03) | 0.96(0.04) | 0.27(0.01) | 0.82(0.02) | 113.5° | 0.70 | 2.37E-2 | (2,6) |
| *8 April 2001 (38.0°N, 133.6°E; 0145 UTC)* | | | | | | | | |
| 0.31(0.01) | 1.33(0.01) | 1.00(0.05) | 0.29(0.08) | 0.83(0.02) | 151.9° | 0.70 | 1.72E-2 | (2.3,8.6) |
| *10 April 2001 (37.9°N, 130.8°E; 0135 UTC)* | | | | | | | | |
| 0.69(0.02) | 1.11(0.02) | 0.82(0.01) | 0.41(0.08) | 0.74(0.01) | 141.5° | 0.69 | 2.14E-2 | (2.6,8.6) |
| *12 April 2001 (35.0°N, 130.0°E; 0300 UTC)* | | | | | | | | |
| 0.65(0.03) | 0.47(0.05) | 0.23(0.03) | 1.12(0.07) | 0.44(0.04) | 108.5° | 0.73 | 1.63E-2 | (3,9) |
| *12 April 2001 (33.1°N, 127.5°E; 0300 UTC)* | | | | | | | | |
| **0.44(0.01)** | **0.59(0.01)** | **0.35(0.04)** | **0.58(0.03)** | **0.54(0.01)** | **113.0°** | **0.73** | **9.00E-3** | **(3,9)** |
| *13 April 2001 (35.7°N, 132.5°E; 0205 UTC)* | | | | | | | | |
| 0.24(0.01) | 1.14(0.03) | 0.29(0.01) | 0.36(0.01) | 0.71(0.01) | 155.5° | 0.69 | 2.21E-2 | (1,9) |
| *13 April 2001 (35.8°N, 132.4°E; 0205 UTC)* | | | | | | | | |
| **0.25(0.01)** | **1.13(0.03)** | **0.28(0.01)** | **0.36(0.01)** | **0.70(0.01)** | **155.9°** | **0.68** | **1.30E-2** | **(1,9)** |
| *14 April 2001 (32.3°N, 132.5°E; 0250 UTC)* | | | | | | | | |
| **1.10(0.18)** | **0.58(0.01)** | **0.36(0.11)** | **0.75(0.11)** | **0.47(0.05)** | **111.1°** | **0.72** | **6.00E-3** | **(3,9)** |
| *15 April 2001 (32.4°N, 128.5°E; 0155 UTC)* | | | | | | | | |
| 0.15(0.03) | 1.24(0.07) | 0.48(0.03) | 0.25(0.04) | 0.79(0.07) | 150.6° | 0.69 | 1.88E-2 | (1.2,8.2) |
| *19 April 2001 (33.1°N, 135.2°E; 0130 UTC)* | | | | | | | | |
| 0.30(0.01) | 1.46(0.04) | 1.20(0.01) | 0.23(0.01) | 0.86(0.01) | 151.7° | 0.70 | 2.08E-2 | (2,8) |
| *19 April 2001 (37.2°N, 133.4°E; 0130 UTC)* | | | | | | | | |
| **0.40(0.01)** | **1.37(0.01)** | **1.04(0.02)** | **0.25(0.03)** | **0.83(0.01)** | **144.1°** | **0.69** | **1.40E-2** | **(2,8)** |
| *20 April 2001 (35.0°N, 140.6°E; 0210 UTC)* | | | | | | | | |
| **0.32(0.02)** | **1.10(0.07)** | **0.75(0.04)** | **0.24(0.06)** | **0.79(0.08)** | **114.2°** | **0.69** | **1.68E-2** | **(1.5,6)** |
| *23 April 2001 (32.4°N, 139.6°E; 0105 UTC)* | | | | | | | | |
| **0.28(0.01)** | **0.99(0.02)** | **0.27(0.05** | **0.27(0.01)** | **0.75(0.01)** | **147.8°** | **0.70** | **1.10E-2** | **(1,8)** |
| *23 April 2001 (33.1°N, 134.1°E;0245 UTC)* | | | | | | | | |
| **0.27(0.03)** | **0.88(0.17)** | **0.62(0.07)** | **0.44(0.10)** | **0.67(0.02)** | **111.4°** | **0.71** | **1.50E-2** | **(2.5,7.5)** |

[a]Here $\tau_{0.55\,\mu m}$, aerosol optical depth at 0.55 μm; $\alpha_{0.66-0.86\mu m}$ μm, Angstrom exponent derived between 0.66 and 0.86 μm; $\alpha_{0.86-2.13}$ μm, Angstrom exponent between 0.86 and 2.13 μm; $r_{eff}$, effective radius; $\eta_{0.55\,\mu m}$, fine-mode fraction at 0.55 μm; $\Theta$, scattering angle; $\psi_{0.55\,\mu m}$, asymmetric factor at 0.55 μm; $\varepsilon$, least square fitting error; modes (fine, coarse), fine and coarse mode aerosol model selected (models 1–2: wet water soluble (0.10 and 0.15 μm effective radius), models 3–4, water soluble with humidity (0.20 and 0.25 μm)); models 5–7, wet sea salt (0.98, 1.48, 1.98 μm); and models 8–9, dust (1.48 and 2.5 μm)).

in the parenthesis) include Jeju Island (1) and Anmyon Island (2), South Korea, and Noto (3), Japan. Note that in the process we have increased the windows in space and time by a factor 2 (i.e., ±50 km instead of ±25 km and ±1 hour instead of ±30 min as for $\tau_a$ validation) in order to accommodate more coincidences.

[22] It is clear to see that MODIS underestimates $r_{eff}$ AERONET retrievals by approximately 20% (see Figure 8). Because the spherical AERONET retrievals are self-affected by nonsphericity and will underestimate true $r_{eff}$ [*Dubovik et al.*, 2000, 2002], MODIS may actually underestimate aerosol effective radius even more severely. In previous comparisons between MODIS- and AERONET-derived $r_{eff}$ when fine-mode aerosols dominated the atmospheric column, good agreement between the two retrieval methods was found [*Remer et al.*, 2002], whereas in dust-dominated situations, in PRIDE (Puerto Rico Dust Experiment) 2000, MODIS was found to underestimate $r_{eff}$ by up to 50% [*Levy et al.*, 2003]. In the six cases of our comparisons in ACE-Asia, we have a situation where dust aerosol resides
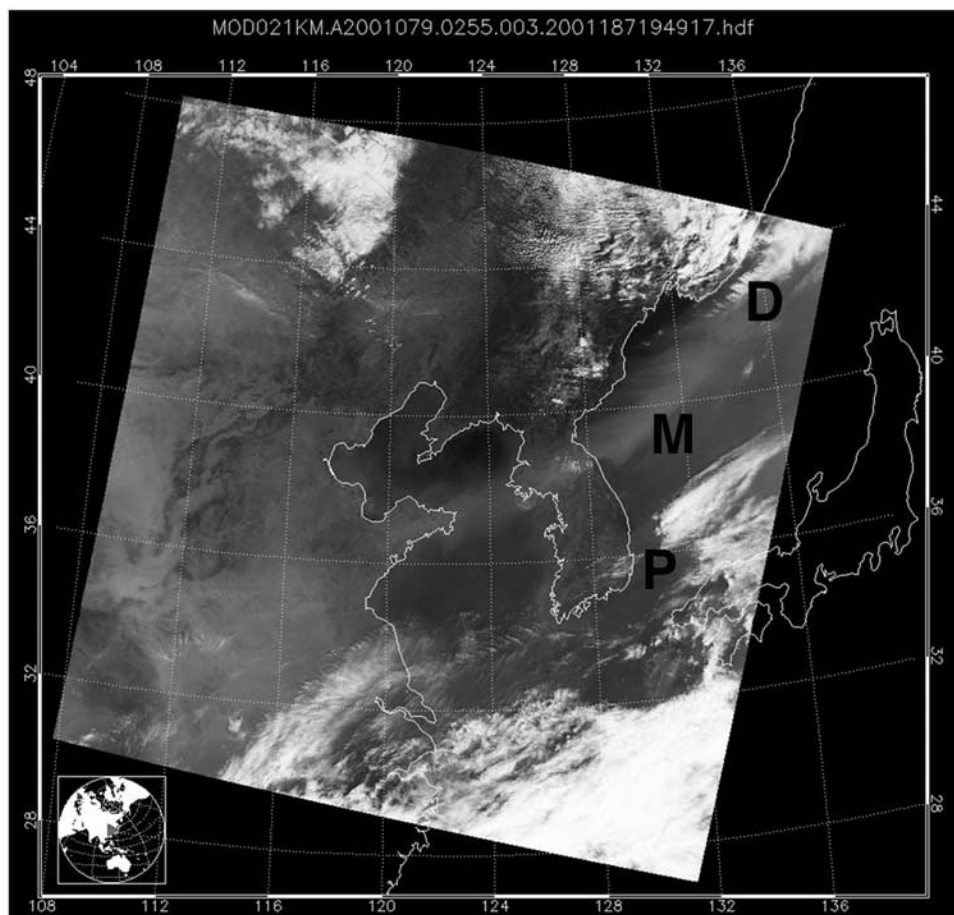
**Figure 10.** MODIS RGB (R, 0.66 μm; G, 0.55 μm; B, 0.47 μm) image of 20 March 2001 (0255 UTC) with dust plume passing through the Korea Peninsula. Three-square boxes (2° × 2°) are chosen to represent dust-dominated, mixed, and pollution-influenced regions.

in an upper layer with a pollution layer below, with neither aerosol type dominating. Thus the degree of underestimation between that and those observed in the two previous studies is reasonable. The underestimation of particle size is associated with MODIS overestimations of spectral curvature. Such was the result of the PRIDE analysis [*Levy et al.*, 2003], and likewise here by exaggerated spectral dependence as seen in Figure 6. However, our results differ from the results from PRIDE in that not only do we see an enhanced spectral dependence from MODIS retrievals, but also an elevated retrieved aerosol optical thickness throughout the entire spectral range. In PRIDE, midvisible values (0.67 μm) of $\tau_a$ from MODIS agreed well with AERONET observations. Another factor to consider is the possibility of sensor calibration issues that affect retrievals in the ACE-Asia period but not in PRIDE.

## 6. Consistency/Relationship of MODIS-Derived Aerosol Size Parameters

[23] The retrieved aerosol size parameters, Ångström exponents, η, and $r_{eff}$ from the 17 events (sections 4.1 and 4.2) are further analyzed to examine the consistency/relationship of derived size parameters and their correspondence to model selections under dust-free to high dust loading conditions (Table 6). First, we derive the correlation between fine-mode fraction and Ångström exponents, and find a very high positive correlation (R∼0.96) between Ångström exponent 1 (0.66 and 0.86 μm; hereinafter, AE1) and η (at 0.55 μm) (see Figure 9a) but moderate negative correlation (R∼−0.7) between Ångström exponent 2 (0.86 and 2.1 μm; hereinafter, AE2) and 1 − η (or coarse-mode fraction) (see Figure 9b). The poorer correlation is primarily caused by outliers with η between 0.7 and 0.8 in cases 9, 10, and 16 associated with low $\tau_a$ ∼0.2−0.3 (0.55 μm) and low AE2 values (∼0.2−0.3) as well as in case 12 with an even lower $\tau_a$ (∼0.15) but a slightly larger AE2 ∼0.48.

[24] The inverse correlation (R∼−0.92) between $r_{eff}$ and η reveals two groups clearly separated by η∼0.6 and $r_{eff}$ ∼0.5 (Figure 9c). The first group includes cases 7, 8, and 11 (dominated by dust) with effective radius > 0.55 μm and fine-mode fraction < 0.6, and the second includes cases 9, 10, and 16, and others with effective radius < 0.55 μm and fine-mode fraction > 0.6 The latter can be further divided by the ratio of AE1/AE2 (>2) as a function of fine-mode fraction (see Figure 9d) with one showing nonlinear spectral variation with large AE1 accompanied by small AE2 (cases 9, 10, 12, and 16) and a good inverse
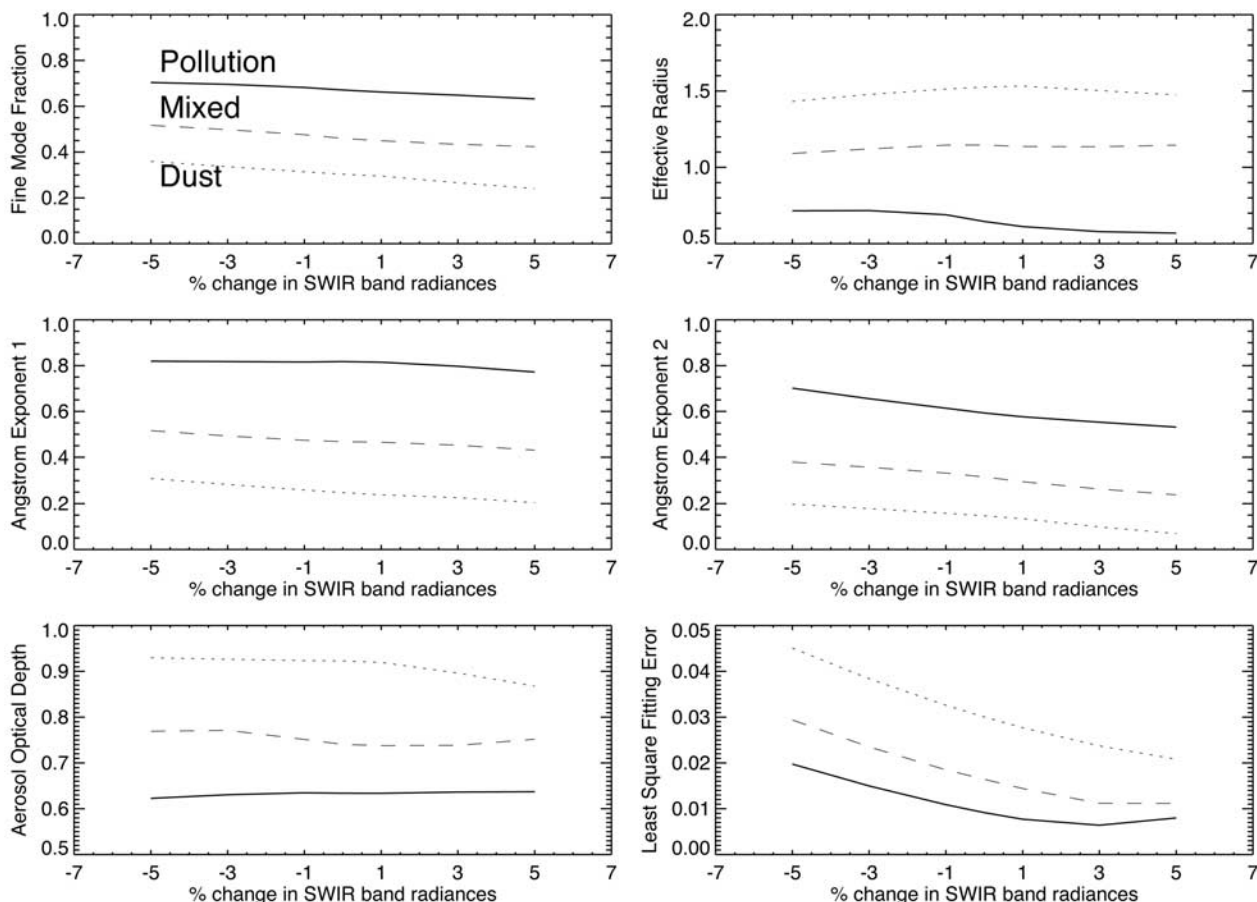
**Figure 11.** Variations of MODIS-derived $\eta$, $r_{eff}$, AE1 (0.55 and 0.87 $\mu$m; hereinafter referred to as AE1) and AE2 (0.87 and 2.1 $\mu$m), $\tau_a$ (0.55 $\mu$m), and $\varepsilon$ (least square fitting error) as a function of percent change (−5−5%) in the SWIR band radiances.

correlation between AE1/AE2 and $\eta$, and another showing AE1/AE2 ~1−2 but with nearly no dependence upon $\eta$ (cases 1−8, 11, 13−15, and 17) (Figure 9d). In the scatterplot of AE2 vs. AE1, cases 2 and 3 with similar AE2 and AE1 are separated from cases 9, 10, 12, and 16 with AE1 being 2−3 times AE2 at the opposite side of the regression line (Figure 9e).

[25] The analysis depicts outstanding cases dominated by dust outbreak (7, 8, 11) and pollution (9, 10, 12, 16). The former uniformly correspond to models 3 and 9 and the latter to models 1 (or 2) and 8 (or 9). Though similarities are shown in cases 2 and 3 in comparison to 9, 10, 12, and16, slight spectral curvature variations differ their fine-mode model selection of 3 (or 4) over 1 (or 2), with respect to particle size, that humidification may play a role. The remainder of the cases (1, 4, 5, 6, 13, 14, 15, 17) behaves spectrally alike regardless of aerosol models selected. In summary, except for cases 4 and 15 with chosen model (6) and cases 1 and 17 with mixed sea-salt (7) and dust (8) modes, dust models (8 and 9) are mostly chosen in combination with water-soluble models, which makes sense in the springtime environment in east Asia. However, this analysis also suggests that the selection of fine and coarse models is sensitive to spectral curvature of measured radi-

ances from visible to SWIR. Any changes in radiances, such as that might be caused by the electronic cross talk in MODIS SWIR bands, can alter spectral curvature and consequently the estimation of $\eta$ and $r_{eff}$.

## 7. Sensor Calibration Issues

[26] It is known from prelaunch and on-orbit sensor characterization that MODIS SWIR bands (detectors)' responses are significantly contaminated by the out-of-band thermal leak and electronic cross talk [*Xiong et al.*, 2004]. Because of this, a simple linear correction algorithm has been designed and applied in the L1B to remove the thermal leak and partially reduce the electronic cross talk. The former is mainly caused by the spectral response functions that do not have clear cutoff allowing radiances of 3−5 $\mu$m bands to penetrate through, which is mostly removed by the contrast to nighttime measurements. The latter is more complex in nature by imperfect resets of SWIR band detectors of subframe (500 m resolution) scanning, which are side-dependent and typically nonlinear and thus scene-dependent. Though different sets of correction coefficients have been applied in the L1B, the remaining effects on the retrieved radiances of the SWIR bands might still be
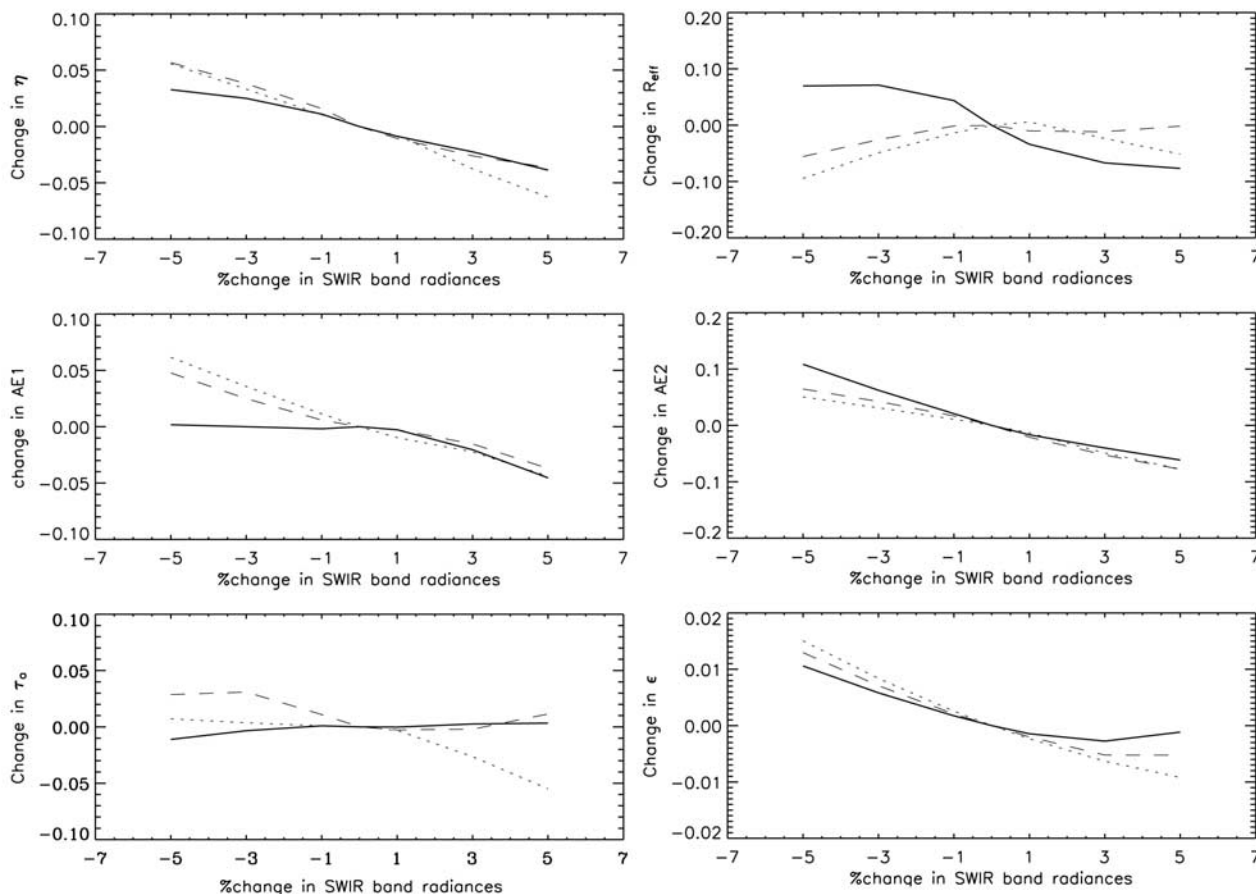
**Figure 12.** Changes of MODIS-derived $\eta$, $r_{eff}$, AE1 (0.55 and 0.87 $\mu$m; hereinafter referred to as AE1) and AE2 (0.87 and 2.1 $\mu$m), $\tau_a$ (0.55 $\mu$m), and $\varepsilon$ (least square fitting error) as a function of percent change ($-5-5\%$) in the SWIR band radiances.

different for side A and side B electronics configurations. The SWIR bands are particularly important to the retrieval of aerosol size parameters in the MODIS algorithm. In analyzing MODIS aerosol size parameters in a long time series, we see a definite discontinuity in aerosol size corresponding to the date when the sensor's electronics package was switched from side B back to side A [*Remer et al.*, 2005]. Here we demonstrate the sensitivity of the aerosol retrieval to slight variations in SWIR band radiances that represent the uncertainty that might remain uncorrected from electronic cross talk artifacts.

[27] We impose a uniform $\pm5$, $\pm3$ and $\pm1$ percent changes on the radiances of MODIS SWIR bands (i.e., 1.24, 1.64, and 2.1 $\mu$m), and calculate the respective changes to a variety of aerosol conditions. The case chosen for the sensitivity study is shown in Figure 10 with a dust plume passing over Korea Peninsula on 20 March 2001 (0255 UTC). The three $2° \times 2°$ regions marked with aerosol loading in the range of 0.6– 0.9 represent dust-dominated, pollution-influenced, and dust/pollution mixed aerosols. Figure 11 shows, respectively, the retrieved $\eta$, $r_{eff}$, AE1 (0.55 and 0.87 $\mu$m) and AE2 (0.87 and 2.1 $\mu$m), $\tau_a$ (0.55 $\mu$m), and $\varepsilon$ (least square fitting error) as a function of percent change ($-5\%$ to 5%) in the SWIR band radiances. To clearly illustrate the response

of the retrieval to radiance perturbation, both absolute (Figure 12) and percent changes (Figure 13) are presented.

[28] It is interesting to learn the irregular changes of $\tau_a$ in the three regions with nearly all negative response of $-6$ to $+1\%$ (or $-0.05$ to $+0.01$) in the dust-dominated, all positive 0 to $+4\%$ (or 0 to 0.03) in the mixed, and within $\pm2\%$ (or $-0.01$ to $+0.01$) in the pollution-influenced region in response to the change in SWIR radiances. The least square fitting errors are also different in the three regions (0.02– 0.05 in the dust-dominated, 0.01–0.03 in the mixed and 0.005–0.02 in the pollution-influenced) but with similar trends of larger errors in the decreasing as opposed to increasing changes of SWIR radiances. On average, these changes are at maximum 1% (or 0.012) with respect to 1% change in radiance, which is smaller than the retrieval uncertainties of $\Delta\tau_a = \pm0.03 \pm 0.05\tau_a$. Thus it can be concluded that the retrieval of $\tau_a$ is not affected by the change in SWIR radiances.

[29] Weaker signals in SWIR bands correspond to less contribution from coarse mode particles and as a result an increased $\eta$ and vice versa. The percent changes in Ångström exponents are consistent with those found in $\eta$. The different magnitudes derived (the largest in the dust-dominated, followed by the mixed and pollution-influenced
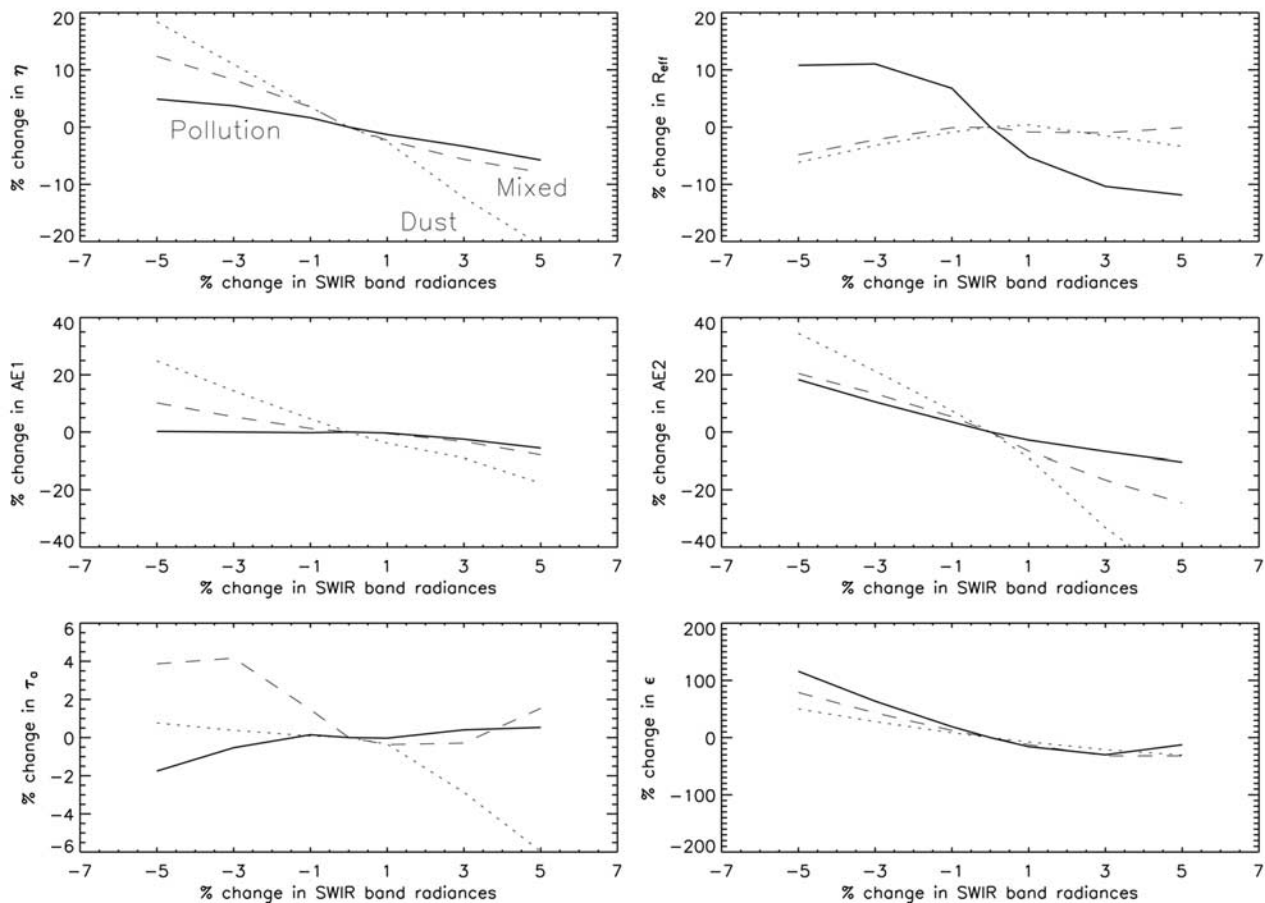
**Figure 13.** Percent changes of MODIS-derived $\eta$, $r_{eff}$, AE1 (0.55 and 0.87 $\mu$m; hereinafter referred to as AE1) and AE2 (0.87 and 2.1 $\mu$m), $\tau_a$ (0.55 $\mu$m), and $\varepsilon$ (least square fitting error) as a function of percent change ($-5-5\%$) in the SWIR band radiances.

region) are related to the spectral curvature of radiances and aerosol model selection, which is clearly seen in the results of $r_{eff}$ that they do not necessarily conform to the changes in $\eta$, i.e., larger $\eta$ leading to smaller the $r_{eff}$, except in the mixed dust/pollution region. The aerosol model selection is believed to play a determinant role since slight perturbation is able to cause a switch between aerosol models (see Figure 14) resulting in increased or decreased $r_{eff}$ not corresponding to $\eta$. It is worth noting here that the aerosol models used in the retrieval can be characterized in size: 1–2: wet water-soluble aerosol (0.10 and 0.15 $\mu$m effective radius), 3–4: water-soluble aerosol with humidification (0.2 and 0.25 $\mu$m), 5–7: wet sea salt (0.98, 1.48, 1.98 $\mu$m), and 8–9: dust (1.48 and 2.5 $\mu$m). In the dust-dominated region, the decrease in SWIR radiance tends to cause the switch of models 2 and 3 to model 4 (humidified and larger particles $\sim$0.25 $\mu$m), and increasing SWIR radiance tends to shift toward models 1, 2, and 3 (less humidified and smaller particles), while the coarse-mode model remains to be dust model 9. Similar trend is also found in the mixed pollution/dust as in the dust-dominated region. In the pollution-influenced region, however, differences are shown in both fine- and coarse-mode model selections that more fine and coarse mode models were selected with increasing as opposed to decreasing changes in SWIR radiances. The

more number of models chosen mean multiple combinations are possible to satisfy similar measurements with subtle spectral variations.

[30] Though we do not show the results for cases of background maritime aerosol (sea salt), it is certain that even larger impacts are expected in $\eta$ and $r_{eff}$ than those found in the dust-dominated case because of less abundant fine-mode aerosols over remote pristine oceans.

## 8. Statistical Analysis on Effect of Side A and Side B Electronics

[31] The sensitivity study has shown the effect of electronic cross talk on the retrievals varying with aerosol types. In the end of October 2000, Terra-MODIS sensor electronics was switched from side A to side B and later switched back to side A in July 2001. The ACE-Asia field campaign occurred exactly after the switch from side A to side B electronics. Though after the switch, the MODIS calibration team reexamined the measured radiances and corrected them to within the baselined ($\pm$5%) error [*Guenther et al.*, 2002], discontinuities are seen in aerosol size parameters. Owing to the complexity of electronic cross talk in nature (i.e., scene-dependent and side-dependent), detailed study will require a comprehensive examination of all possible
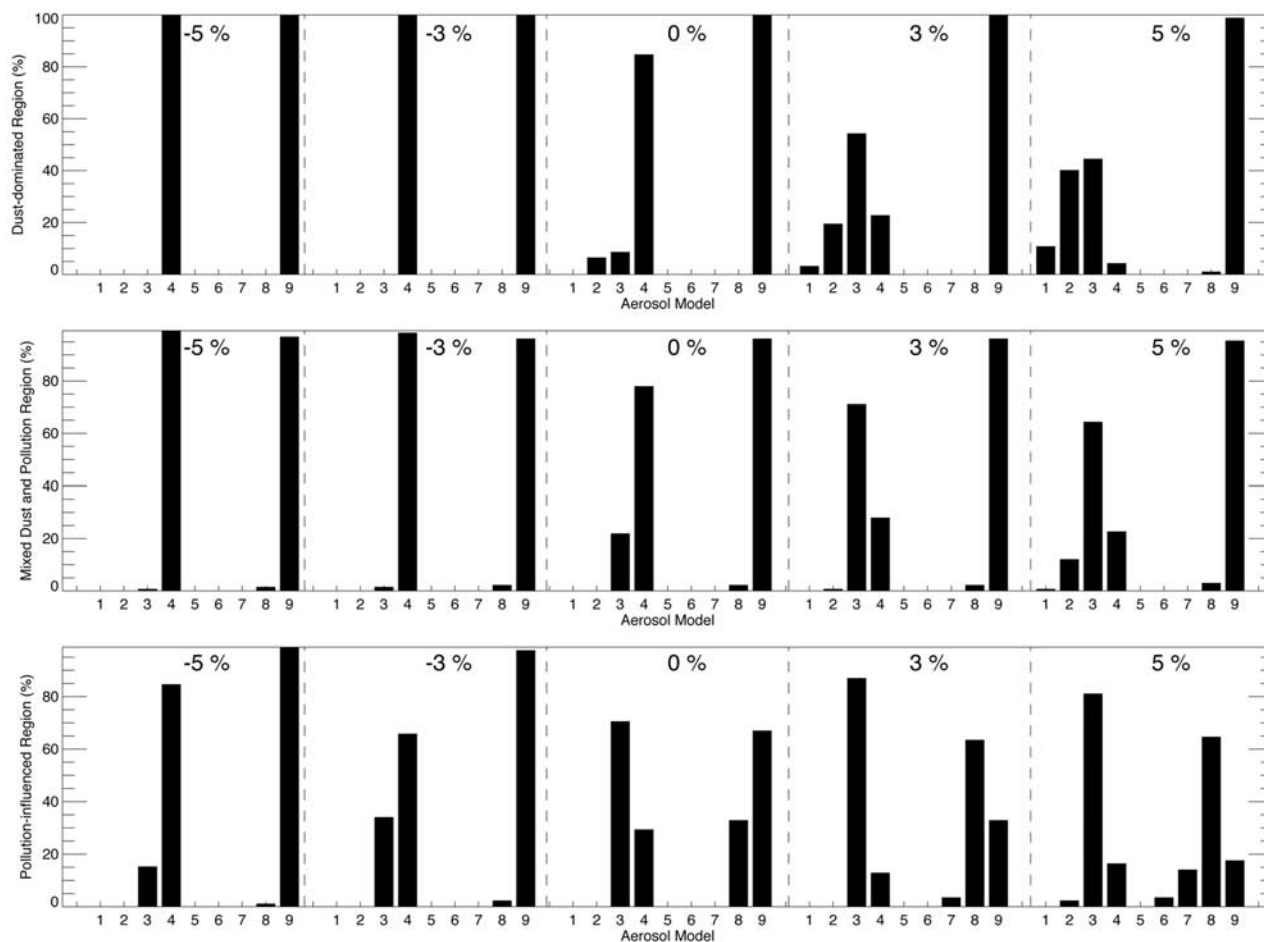
**Figure 14.** Aerosol model selection in response to percent change (−5%, −3%, 3%, and 5%) in the SWIR band radiances.

scenarios. We have formed a plan to do that in collaboration with MODIS calibration team based upon the findings of this paper.

[32] In this section, we compare MODIS level 3 1° × 1° aerosol products in the three dust outbreak seasons (March–May) of 2000, 2001, and 2002 over the area from 100° to 160° longitude and 10° to 60° latitude as shown earlier in section 3. The year 2000 represent the data before the switch and 2002 the data after the switch back. These three seasons are comparable because of reportedly similar numbers of dusty days in northern China. The exclusion of year 2003 is due to significantly less number of dust outbreaks (∼3 times) in that year as attributed to heavy snowfalls in the deserts and neighboring regions, preventing the formation of dust storms. Figure 15 shows the scatterplots of regional monthly mean $r_{eff}$ and $\eta$ (left panel) and $r_{eff}$ and $\tau_a$ (right panel) of the 20 (10° × 10°) regions from March to May of 2000, 2001 and 2002. Aerosol loading, $\tau_a$, is least affected by the cross talk as shown in sensitivity study (section 7). As a result, the range of $\tau_a$ appears to be no different between 2000, 2001, and 2002 data. However, the effect is much more pronounced on the size parameters (i.e., $\eta$, $r_{eff}$). First, we can see overall a lower range of $r_{eff}$ (0.2–0.8 μm) and higher range $\eta$ (0.4–0.9) of 2001 data compared to those of 2000 ($r_{eff}$: 0.2–1.3 μm and $\eta$: 0.1–

0.9) and 2002 ($r_{eff}$: 0.2–1.2 μm and $\eta$: 0.2–0.9) data. Second, the missing coarse mode (>1 μm) of monthly $r_{eff}$ histogram in region 20 over remote pristine oceans (dominated by sea salt) is evident that $r_{eff}$ values obtained from side A are underestimated (see Figure 16). We excluded interannual variability since it should only change the intensity, not the range, of the parameters given such a large area.

[33] In summary, about 80% of the points from side B (2001) retrievals are fallen within the range of $r_{eff}$ between 0.3 and 0.5 μm in corresponding to $\tau_a$ ∼0.15–0.9. Larger values of $r_{eff}$ ∼0.6–0.8 μm (or 0.45–0.55 in $\eta$) are only seen for $\tau_a \leq 0.1$ (Figure 15). By comparing the monthly mean $r_{eff}$ of side B retrievals in 2001 to those of the side A retrievals in 2000 and 2002, it can be estimated that the $r_{eff}$ values in ACE-Asia are ∼100% smaller for $\tau_a \leq 0.10$, 50–60% for $\tau_a$ ∼0.1–0.3, 20–30% for $\tau_a$ ∼0.3–0.5, and 10–15% for $\tau_a \geq 0.5$.

## 9. Concluding Remarks

[34] Aerosol retrievals from MODIS provide a wide regional view of aerosol loading and particle size across the northwestern Pacific during the ACE-Asia field experiment in spring 2001. In general, there is a decrease in $\tau_a$
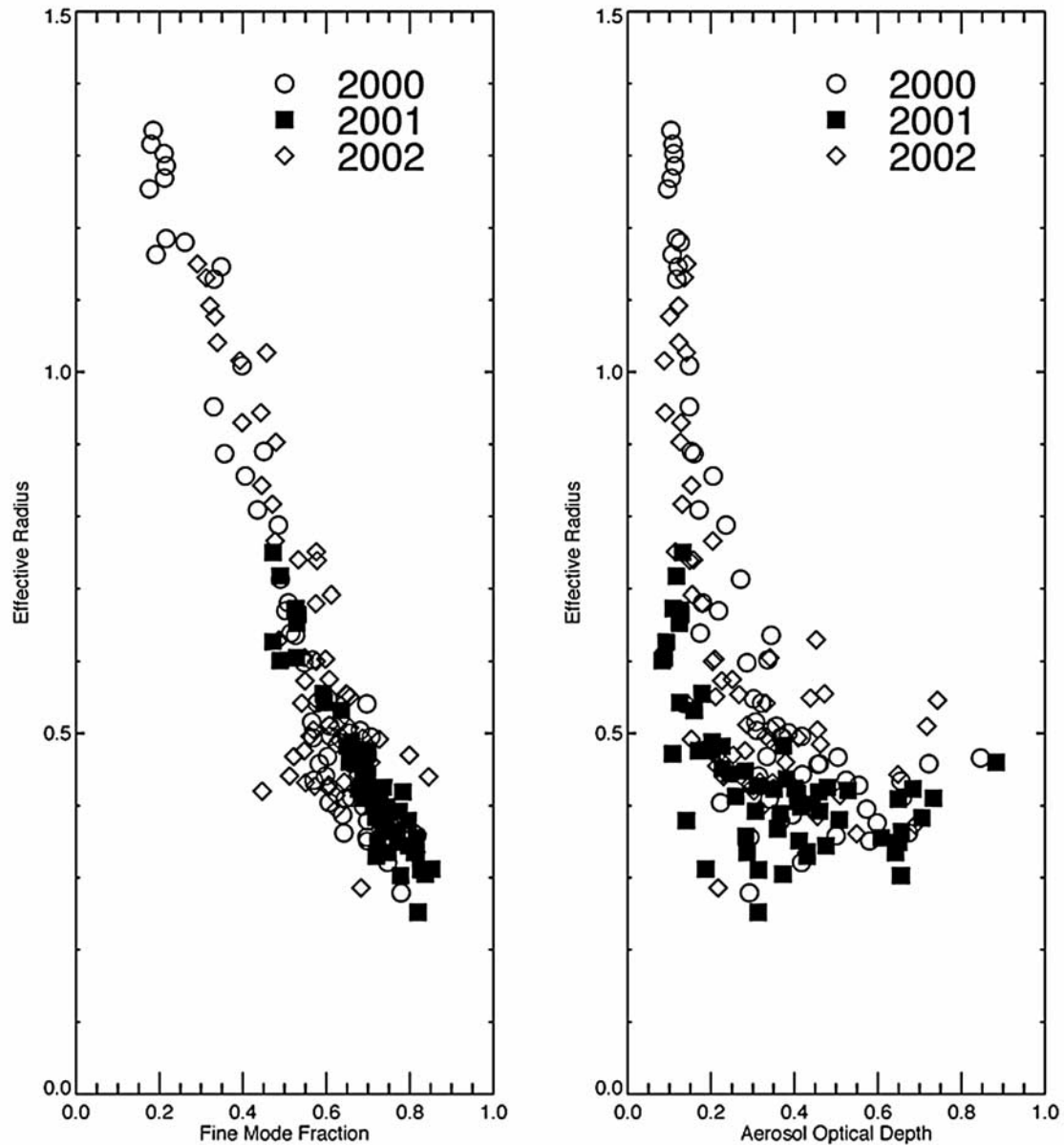
**Figure 15.** Scatterplots of regional monthly means of (left) $r_{eff}$ and $\eta$ and (right) $r_{eff}$ and $\tau_a$ of 20 regions from March to May in 2000, 2001, and 2002.

with the distance eastward from the Asian continent. The highest aerosol loading (monthly mean $\tau_a \sim 0.40-0.70$) occurs in the belts associated with periodic dust transport events ($30°-50°N$). The lowest aerosol loading (monthly mean $\tau_a \sim 0.08-0.12$) occurs in the southeastern edges of our domain ($10°-20°N$; $150°-160°E$). The monthly mean $\eta$ varies between approximately 0.5 in the cleanest regions to approximately 0.8 in near the coast of Southeast Asia
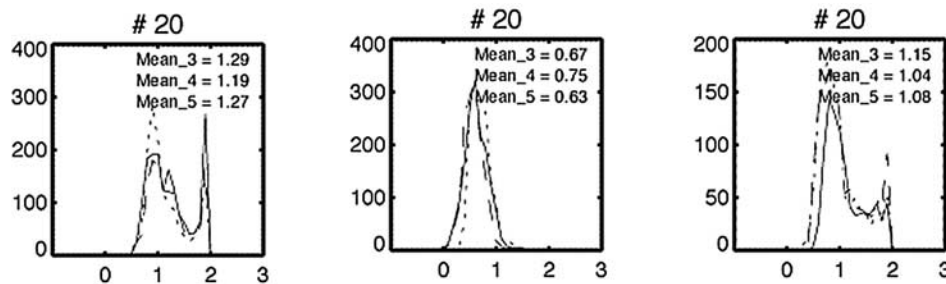


**Figure 16.** Histogram of regional monthly $r_{eff}$ in region 20 of March (solid line), April (dotted line), and May (dashed) of (left) 2000, (middle) 2001, and (right) 2002.

dominated by biomass burning smoke. Conversely, the monthly mean $r_{eff}$ ranges between approximately 0.8 and 0.3 μm.

[35] The validation of $\tau_a$ in ACE-Asia leads to similar conclusions as obtained from the globe and from different parts of the world ($\Delta\tau_a = \pm0.03 \pm 0.05\tau_a$). The collection 4 MODIS-derived $\tau_a$ values in ACE-Asia are in good agreement (SRMSE ≤0.05) with spaceborne and shipborne Sun photometer/radiometers (AATS-14, AATS-6, Microtops, Simbad, SimbadA, and shadowband radiometer) in the absence of dust, and consistently larger errors across the spectrum (0.47–2.1 μm) are found during dust outbreaks (SRMSE ~0.1–0.3). Aerosol loading is least affected by electronic cross talk as shown by the sensitivity study (within ±0.05). Dust nonsphericity is considered to be responsible for the overestimated aerosol loading.

[36] The MODIS-derived regional monthly η range (0.4–0.9) during ACE-Asia in 2001 is higher than the range found in the same region in 2000 (0.1–0.9) and in 2002 (0.2–0.9). Conversely, the MODIS-derived $r_{eff}$ is lower in 2001 (0.2–0.8 μm) than in 2000 (0.2–1.3 μm) or in 2002 (0.2–1.2 μm). Sensitivity studies depict that the variation in the SWIR band radiances on the order of expected residual cross talk can change aerosol model selections in the retrieval, and introduce errors to aerosol size parameters. The effect of electronic cross talk is greater for low aerosol loading (e.g., remote pristine ocean) and also for dust- than pollution-dominated conditions. The missing coarse mode (>1 μm) of the monthly mean $r_{eff}$ in remote pristine oceans ($\tau_a < 0.15$) is evident for the anomalies of retrievals from side B as opposed to side A electronics. Collectively, about 80% of the points (regional monthly means from March to May) from side B (2001) retrievals fall within the range of $r_{eff}$ between 0.3 and 0.5 μm in corresponding to $\tau_a$ ~0.15–0.9; large values of $r_{eff}$ ~0.6–0.8 μm are only seen for $\tau_a \leq$ 0.1. It is an artifact most likely resulted from electronic cross talk in the SWIR bands rather than interannual variability since interannual variability should only change the intensity, not the range, of the parameters. The $r_{eff}$ values derived in ACE-Asia can be estimated ~100% smaller for $\tau_a \leq 0.10$, 50–60% for $\tau_a$ ~0.1–0.3, 20–30% for $\tau_a$ ~0.3–0.5, and 10–15% for $\tau_a \geq 0.5$.

[37] Owing to the nature of scene-dependent electronic cross talk, the correction set at one level may not be adequate for another. Unless MODIS electronic cross-talk effects can be completely removed or fully characterized, the evaluation of the uncertainties of MODIS-retrieved aerosol size parameters remains inconclusive in ACE-Asia, and may be largely the case for the entire period of side B electronics.

## References

Ackerman, S. A., et al. (1998), Discriminating clear-sky from clouds with MODIS, *J. Geophys. Res.*, 103, 32,141–32,158.

Andreae, M. A. (1996), Raising dust in the greenhouse, *Nature*, 380, 389–390.

Carlson, T. N., and S. G. Benjamin (1980), Radiative heating rates for Saharan dust, *J. Atmos. Sci.*, 37, 193–213.

Chou, M.-D., P.-K. Chan, and M. Wang (2002), Aerosol radiative forcing derived from SeaWiFS-retrieved aerosol optical properties, *J. Atmos. Sci.*, 59(3), 748–757.

Chu, D. A., Y. J. Kaufman, L. A. Remer, and B. N. Holben (1998), Remote sensing of smoke from MODIS airborne simulator during the SCAR-B experiment, *J. Geophys. Res.*, 103, 31,979–31,987.

Chu, D. A., K. I. Strabola, S. Planick, E. Moody, M. D. King, S. Mattoo, and B. Ridgway (2002), MODIS atmosphere QA plan, EOS Proj. Off., NASA Goddard Space Flight Cent., Greenbelt, Md. (Available at http://modis-atmos.gsfc.nasa.gov.)

Chu, D. A., Y. J. Kaufman, G. Zibordi, J. D. Chern, J. Mao, C. Li, and B. N. Holben (2003), Global monitoring of air pollution over land from the Earth Observing System-Terra Moderate Resolution Imaging Spectroradiometer (MODIS), *J. Geophys. Res.*, 108(D21), 4661, doi:10.1029/2002JD003179.

Dentener, F. J., G. Carmichael, Y. Zhang, J. Lelieveld, and P. J. Crutzen (1996), Role of mineral aerosol as reactive surface in the global troposphere, *J. Geophys. Res.*, 101, 22,869–22,889.

Deschamps, P. Y., B. Fougnie, R. Frouin, P. Lecomte, and C. Verwaerde (2004), SIMBAD: An advanced field radiometer to measure aerosol optical thickness and marince reflectance, *Appl. Opt.*, 43(20), 4055–4069.

Dubovik, O., and M. D. King (2000), A flexible inversion algorithm for retrieval of aerosol optical properties from Sun and sky radiance measurements, *J. Geophys. Res.*, 105, 20,673–20,696.

Dubovik, O., A. Smirnov, B. N. Holben, M. D. King, Y. J. Kaufman, T. F. Eck, and I. Slutsker (2000), Accuracy assessments of aerosol optical properties retrieved from AERONET Sun and sky radiance measurements, *J. Geophys. Res.*, 105, 9791–9806.

Dubovik, O., B. N. Holben, T. F. Eck, A. Smirnov, Y. J. Kaufman, M. D. King, D. Tanré, and I. Slutsker (2002), Variability of absorption and optical properties of key aerosol types observed in worldwide locations, *J. Atmos. Sci.*, 59, 590–608.

Elliot, S., D. R. Blake, R. A. Duce, C. A. Lai, I. McCreary, L. A. McNair, F. S. Rowland, A. G. Russell, G. E. Streit, and R. P. Turco (1997), Motorization of China implies changes in pacific air chemistry and primary production, *Geophys. Res. Lett.*, 24, 2671–2674.

Gao, B., Y. J. Kaufman, D. Tanre, and R. Li (2002), Distinguishing tropospheric aerosols from thin cirrus clouds for improved aerosol retrievals using the ratio of 1.38-μm and 1.24-μm channels, *Geophys. Res. Lett.*, 29(18), 1890, doi:10.1029/2002GL015475.

Goodman, A. L., G. M. Underwood, and V. H. Grassian (2000), A laboratory study of the heterogeneous reaction of nitric acid on calcium carbonate particles, *J. Geophys. Res.*, 105, 19,053–19,064.

Guenther, B., X. Xiong, V. V. Salomonson, W. L. Barnes, and J. Young (2002), On-orbit performance of the Earth Observing System Moderate Resolution Imaging Spectroradiometer: First year of data, *Remote. Sens. Environ.*, 83, 16–30.

Haywood, J., P. Francis, S. Osborne, M. Glew, N. Loeb, E. Highwood, D. Tanré, G. Myhre, P. Formenti, and E. Hirst (2003), Radiative properties and direct radiative effect of Saharan dust measured by the C-130 aircraft during SHADE: 1. Solar spectrum, *J. Geophys. Res.*, 108(D18), 8577, doi:10.1029/2002JD002687.

Hsu, N. C., J. R. Herman, and C. Weaver (2000), Determination of radiative forcing of Saharan dust using combined TOMS and ERBE data, *J. Geophys. Res.*, 105, 20,649–20,661.

Huebert, B. J., T. Bates, P. B. Russell, G. Shi, Y. J. Kim, K. Kawamura, G. Carmichael, and T. Nakajima (2003), An overview of ACE-Asia: Strategies for quantifying the relationships between Asian aerosols and their climatic impacts, *J. Geophys. Res.*, 108(D23), 8633, doi:10.1029/2003JD003550.

Ignatov, A., L. Stowe, and R. Singh (1998), Sensitivity study of the Angstrom exponent derived from AVHRR over oceans, *Adv. Space Res.*, 21, 439–442.

Jaffe, D., et al. (1999), Transport of Asian air pollution to North America, *Geophys. Res. Lett.*, 26(6), 711–714.

Kahn, R., et al. (2004), Environmental snapshots from ACE-Asia, *J. Geophys. Res.*, 109, D19S14, doi:10.1029/2003JD004339.

Kaufman, Y. J., D. Tanre, L. A. Remer, E. F. Vermote, D. A. Chu, and B. N. Holben (1997), Operational remote sensing of tropospheric aerosol over the land from EOS-MODIS, *J. Geophys. Res.*, 102, 17,051–17,061.

Knobelspiesse, K. D., C. Pietras, and G. S. Fargion (2003), Sun-pointing error correction for area deployment of the Microtops II handheld Sun photometer, *J. Atmos. Ocean. Technol.*, 20(5), 767–771.

Levy, R. C., L. A. Remer, D. Tanré, Y. J. Kaufman, C. Ichoku, B. N. Holben, J. M. Livingston, P. B. Russell, and H. Maring (2003), Evaluation of the Moderate-Resolution Imaging Spectroradiometer (MODIS) retrievals of dust aerosol over the ocean during PRIDE, *J. Geophys. Res.*, 108(D19), 8594, doi:10.1029/2002JD002460.

Li, R. R., Y. J. Kaufman, B. C. Gao, and C. O. Davis (2003), Remote sensing of suspended sediments and shallow coastal waters, *IEEE Trans. Geosci. Remote Sens.*, 41(3), 559–566.

Li, X., H. Maring, D. Savoie, K. Voss, and J. M. Prospero (1996), Dominance of mineral dust in aerosol light scattering in the North Atlantic trade winds, *Nature*, 380, 416–419.

Martins, J. V., D. Tanré, L. Remer, Y. Kaufman, S. Mattoo, and R. Levy (2002), MODIS Cloud screening for remote sensing of aerosols over oceans using spatial variability, *Geophys. Res. Lett.*, 29(12), 8009, doi:10.1029/2001GL013252.

Matsumoto, T., P. B. Russell, C. Mina, W. Van Ark, and V. Banta (1987), Airborne tracking Sun photometer, *J. Atmos. Ocean. Technol.*, 4, 336–339.

Miller, M. A., R. M. Reynolds, and M. J. Bartholomew (2001), Aerosol optical properties over the ocean: A summary of the FRSR data base calibration protocol and measurements uncertainties, Simbios project 2001 annual report, *NASA Tech. Memo. 2002-210005*, pp. 77–82, NASA Goddard Space Flight Cent., Greenbelt, Md.

Mishchenko, M. I., L. D. Travis, R. A. Kahn, and R. A. West (1997), Modeling phase function for dustlike tropospheric aerosols using a shape mixture of randomly oriented polydisperse spheroids, *J. Geophys. Res.*, 102(D14), 16,831–16,847.

Phadnis, M. J., and G. R. Carmichael (2000), Numerical investigation of the influence of mineral dust on the tropospheric chemistry of east Asia, *J. Atmos. Chem.*, 36, 285–323.

Remer, L. A., et al. (2002), Validation of MODIS aerosol retrieval over ocean, *Geophys. Res. Lett.*, 29(12), 8008, doi:10.1029/2001GL013204.

Remer, L. A., et al. (2005), The MODIS aerosol algorithm, products and validation, *J. Atmos. Sci.*, in press.

Shaw, G. E. (1983), Sun photometry, *Bull. Am. Meteorol. Soc.*, 64, 4–11.

Stowe, L., A. Ignatov, and R. Singh (1997), Development, validation, and potential enhancements to the second-generation operational aerosol product at the National Environmental Satellite, Data and Information Service of the National Oceanic and Atmospheric Administration, *J. Geophys. Res.*, 102, 16,923–16,934.

Sun, J., M. Zhang, and T. Liu (2001), Spatial and temporal characteristics of dust storms in China and its surrounding region, 1960–1999: Relations to source area and climate, *J. Geophys. Res.*, 106, 10,325–10,333.

Swap, R., M. Garstang, S. Greco, R. Talbot, and P. Kallberg (1992), Saharan dust in the Amazon basin, *Tellus*, 44(2), 133–149.

Tabazadeh, A., M. Z. Jacobson, H. B. Singh, O. B. Toon, J. S. Lin, R. B. Chatfield, A. N. Thakur, R. W. Talbot, and J. E. Dibb (1998), Nitric acid scavenging by mineral and biomass burning aerosols, *Geophys. Res., Lett.*, 25, 4185–4188.

Tanré, D., Y. J. Kaufman, M. Herman, and S. Mattoo (1997), Remote sensing of aerosol properties over oceans using the MODIS/EOS spectral radiances, *J. Geophys. Res.*, 102, 16,971–16,988.

Tanré, D., L. A. Remer, Y. J. Kaufman, S. Mattoo, P. V. Hobbs, J. M. Livingston, P. B. Russel, and A. Smirnov (1999), Retrieval of aerosol optical depth thickness and size distribution over ocean from MODIS airborne simulator during TARFOX, *J. Geophys. Res.*, 104, 2261–2278.

Tegen, I., and I. Fung (1994), Modeling of mineral dust in the atmosphere: Sources, transport, and optical thickness, *J. Geophys. Res.*, 99, 22,897–22,914.

Tegen, I., and I. Fung (1995), Contribution to the atmospheric mineral aerosol load from surface modification, *J. Geophys. Res.*, 100, 18,707–18,726.

Tegen, I., A. A. Lacis, and I. Fung (1996), The influence on climate forcing of mineral aerosol from disturbed soils, *Nature*, 380, 419–422.

Terada, H., H. Ueda, and Z. Wang (2002), Trend of acid rain and neutralization by yellow sand in east Asia—A numerical study, *Atmos. Environ.*, 36, 503–509.

VanArdeen, G., G. Carmichael, H. Levy, D. Streets, and L. Hordijk (1999), Anthropogenic NOx emission in Asia in the period 1990–2020, *Atmos. Environ.*, 33, 633–646.

Xiong, X., W. L. Barnes, B. Guenther, and R. E. Murphy (2003), Lessons learned from MODIS, *Adv. Space Res.*, 32(11), 2017–2122.

Xiong, X., K. Chiang, W. Li, F. Adimi, H. Yatagai, and W. L. Barnes (2004), The MODIS correction algorithm for out-of-band response in the short-wave IR bands, *Proc. SPIE*, 5234, 605–613.

————————————

J.-D. Chern, D. A. Chu, Y. J. Kaufman, L. A. Remer, and W. Ridgway, Laboratory for Atmospheres, Code 913, NASA Goddard Space Flight Center, Greenbelt, MD 20771, USA. (jchern@agnes.gsfc.nasa.gov; achu@climate.gsfc.nasa.gov; yoram.j.kaufman@nasa.gov; lorraine.a.remer@nasa.gov; ridgway@climate.gsfc.nasa.gov)

K. Knobelspiesse, Laboratory for Hydrology, Code 970.2, NASA Goddard Space Flight Center, Greenbelt, MD 20771, USA. (kirk@simbios.gsfc.nasa.gov)
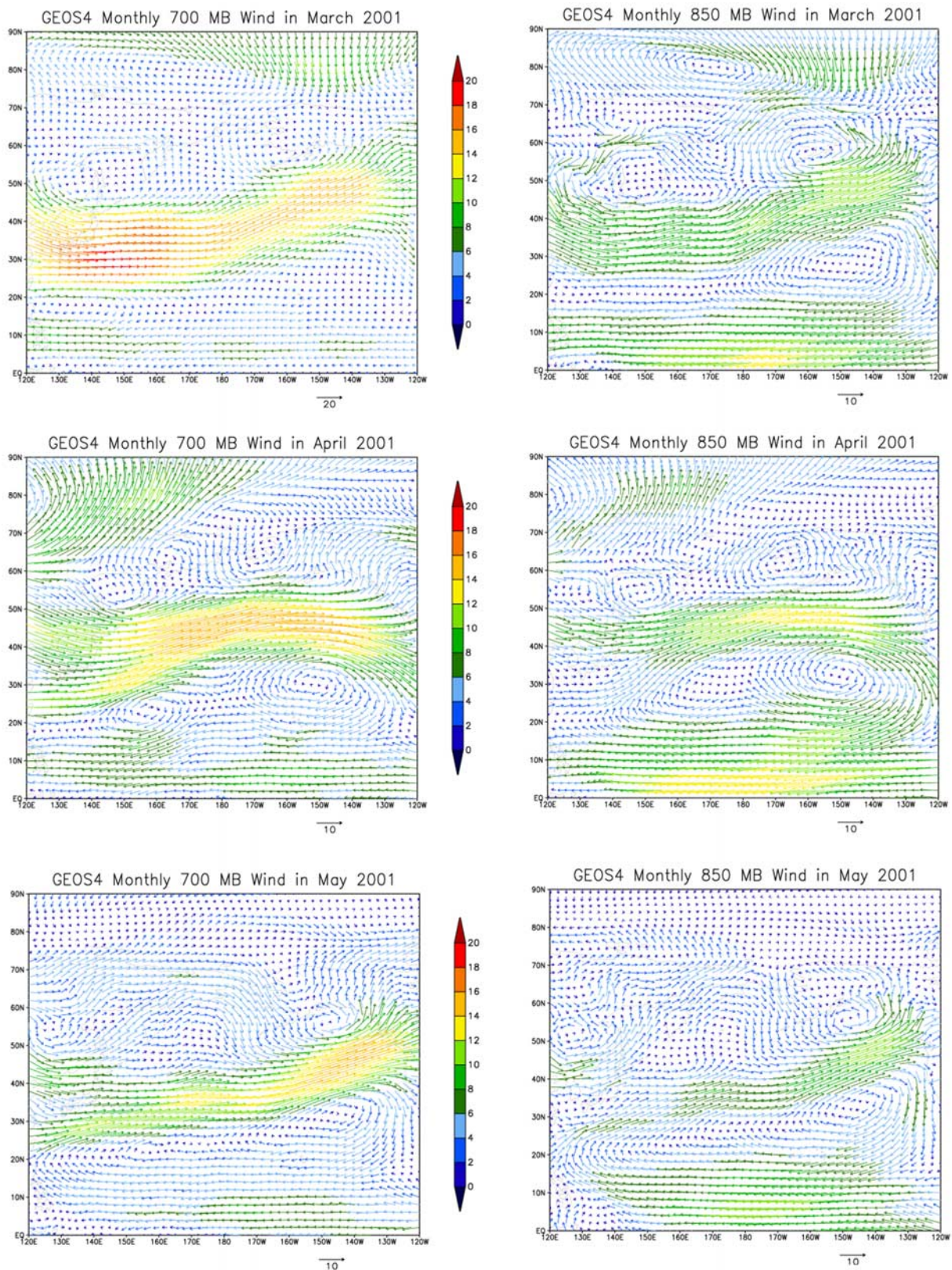
J. Livingston, J. Redemann, P. B. Russell, and B. Schmid, NASA Ames Research Center, MS 245-5, Moffett Field, CA 94035-1000, USA. (jlivingston@mail.arc.nasa.gov; jredemann@mail.arc.nasa.gov; philip.b.russell@nasa.gov; bschmid@mail.arc.nasa.gov)

X. Xiong, Laboratory of Terrestrial Physics, Code 922, NASA Goddard Space Flight Center, Greenbelt, MD 20771, USA. (xiaoxiong.xiong_1@nasa.gov)
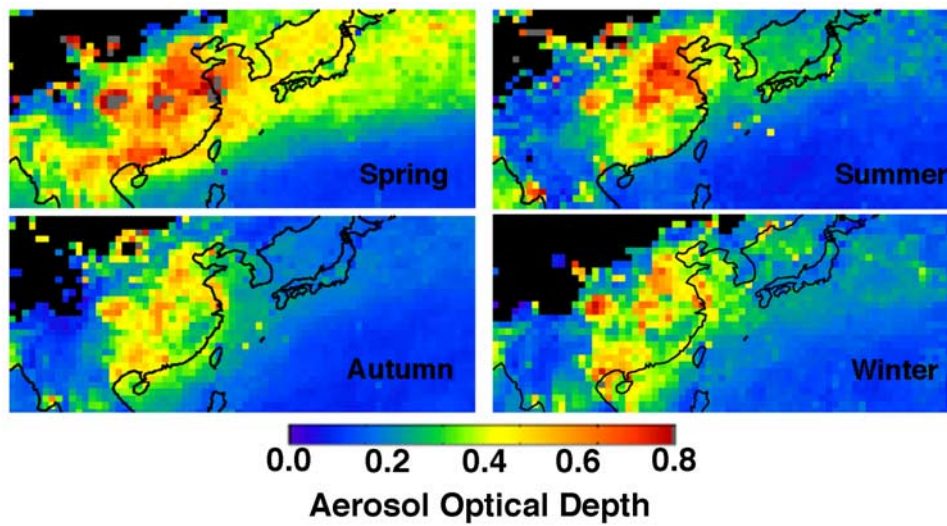
**Figure 1.** Seasonal mean $\tau_a$ in spring, summer, autumn, and winter (December 2000 to November 2001) for the region of $15°-45°N$ and $90°-160°E$.

**Figure 2.** NASA Global Modeling and Assimilation Office (GMAO) (formerly the Data Assimilation Office) assimilated winds at 700 (left column) and 850 mb (right column) for (top) March, (middle) April, and (bottom) May 2001.